Cryo-ET of HIV reveals Env positioning on Gag lattice and structural variation among Env trimers

Vidya Mangala Prasad[1¥], Daniel P. Leaman[4], Klaus N. Lovendahl[1], Jacob T. Croft[1], Mark A. Benhaim[1†], Edgar A. Hodge[1], Michael B. Zwick[4] and Kelly K. Lee[1,2,3*]

1. Department of Medicinal Chemistry, University of Washington, Seattle, WA 98195, USA.
2. Biological Physics, Structure and Design Graduate Program, University of Washington, Seattle, WA 98195, USA.
3. Department of Microbiology, University of Washington, Seattle, WA 98195, USA.
4. Department of Immunology and Microbiology, The Scripps Research Institute, La Jolla, CA 92037, USA

¥Current Address: Molecular Biophysics Unit, Indian Institute of Science, Bengaluru 560012, Karnataka, India.

†Current Address: Alkermes, Inc., 900 Winter St, Waltham, MA 02451, USA.

*Address correspondence to: kklee@uw.edu

Summary:

HIV-1 Env mediates viral entry into host cells and is the sole target for neutralizing antibodies. However, Env structure and organization in its native virion context has eluded detailed characterization. Here we used cryo-electron tomography to analyze Env in mature and immature HIV-1 particles. Immature particles showed distinct Env positioning relative to the underlying Gag lattice, providing insights into long-standing questions about Env incorporation. A 9.1Å sub-tomogram averaged reconstruction of virion-bound Env in conjunction with structural mass spectrometry revealed unexpected features, including a variable central core of the gp41 subunit, heterogeneous glycosylation between protomers plus a flexible stalk that allows Env tilting and variable exposure of neutralizing epitopes. Together, our results provide an integrative understanding of HIV assembly and structural variation in Env antigen presentation.

Keywords: HIV Env glycoprotein, HIV assembly, Gag-Env interaction, Cryo-electron tomography, sub-tomogram averaging, structural mass spectroscopy.

Introduction:

Human Immunodeficiency Virus-1 (HIV-1) continues to infect nearly two million people worldwide each year, with no vaccine available against the virus (Pandey and Galvani 2019). The envelope glycoprotein (Env) on the surface of HIV-1 is an essential viral entry machine that mediates binding to host cell receptors and subsequent membrane fusion. As the sole target for neutralizing antibodies, Env is also of singular importance for vaccine design efforts (van Gils and Sanders 2013). Env is translated as a precursor gp160 protein, which trimerizes, and is cleaved into gp120 and gp41 subunits that are primarily responsible for receptor binding and fusion,

46 respectively. The gp120 and gp41 subunits remain as non-covalently associated heterodimers with
47 gp41 embedded in the viral membrane via its transmembrane domain (TMD) and the C-terminal
48 cytoplasmic domain (CTD) in the viral lumen. Upon incorporation into budding virions, Env CTD
49 interacts with the matrix domain (MA) of immature Gag polyprotein which assembles as a
50 membrane-associated lattice on the inner side of the viral bilayer (Checkley, Luttge et al. 2011,
51 Tedbury and Freed 2014).

52 Recent insights into Env structure have primarily come from studies of engineered,
53 truncated forms of the trimer ectodomain (such as SOSIPs) (Ward and Wilson 2015, Stewart-
54 Jones, Soto et al. 2016), while details of Env structure in its viral membrane context, including its
55 organization relative to other viral components, has remained elusive. In order to understand how
56 Env is assembled on virions and how it differs structurally from soluble trimers, we carried out
57 cryo-electron tomography (cryo-ET) with sub-tomogram averaging, and structural mass
58 spectrometry analysis of Env displayed on immature and mature Gag-bearing HIV-1 virus-like
59 particles. These studies advance our knowledge of membrane-bound Env via insights gained from
60 cryo-ET of intact viral particles.

61

62 **Results and Discussion:**

63 Virion particles bearing ADA.CM Env, a variant of subtype B isolate ADA that was
64 selected for stability (Leaman and Zwick 2013), were produced in human HEK 293T cells as
65 previously described (Stano, Leaman et al. 2017) (Figure 1A, B). These membrane enveloped
66 virus-like particles, referred to as high Env (h)VLPs, display elevated levels of Env trimers that
67 are fully functional for mediating receptor binding and entry. Env on hVLPs retain the antigenic
68 profile of full-length Env (Figure S1 and Table S1), despite a C-terminal truncation of 102 amino

69 acids in the CTD (Stano, Leaman et al. 2017). hVLPs assemble around a functional Gag layer that
70 undergoes proteolytic maturation and have the composition of authentic HIV-1 virions but are
71 replication incompetent because the packaged genome lacks the Env gene (Leaman and Zwick
72 2013, Stano, Leaman et al. 2017). Purified hVLPs were additionally treated with aldrithiol-2 (AT-
73 2), a mild oxidizing agent that interrupts nucleocapsid interaction with RNA, to ensure non-
74 infectivity (Rossio, Esser et al. 1998). Antibody binding experiments showed that the antigenicity
75 of hVLP-Env was unaffected by AT-2 treatment (Figure S2). Despite the lack of infectivity of AT-
76 2 treated hVLPs, they induced syncytia formation and cytotoxicity in cells, similar to non-AT-2
77 treated hVLPs, in accordance with a previous report (Rossio, Esser et al. 1998), showing that AT-
78 2 treated HIV-1 virions bear functional Env that are capable of cell entry (Figure S2). These results
79 indicate that the Env conformation on the hVLPs was not significantly altered by AT-2 as the
80 antigenicity and viral entry properties of Env are retained. The high density of surface Env on
81 hVLPs allowed us to gather sufficient cryo-ET data to obtain a 9.1Å resolution structure of Env in
82 a membrane context on these virus-like particles (Figure 1C and S3).
83
84 **Env structure from immature particles reveal interactions with Gag**
85 Though the hVLPs in our sample population were predominantly mature, approximately
86 3% of the particles appeared immature, exhibiting a clear, assembled Gag lattice beneath the viral
87 membrane (Figure 1A). Env sub-tomogram volumes from only these immature particles were
88 averaged together to give density maps at ~31 Å (C3 symmetry) and ~34 Å (C1 symmetry) (Figure
89 1D and S4). The Env structure from immature particles closely resembles the sub-nanometer Env
90 structure generated from the total hVLP population (Figure 1C) and other reported Env ectodomain
91 structures (Kwon, Pancera et al. 2015, Ward and Wilson 2015). In the averaged immature Env

92 map, a third density layer is seen underneath the membrane bilayer corresponding to the Gag lattice
93 position (Figure 1A, D and Figure S4B, C). Focused refinement of this internal third layer revealed
94 a distinct structure that clearly resembles a lattice formed by the capsid domain (CA) of immature
95 Gag polyprotein (Figure 1E and Figure S4D) (Schur, Hagen et al. 2015). Thus, structures of
96 trimeric Env ectodomain (Pan, Peng et al. 2020) and hexameric Gag-CA (Schur, Hagen et al. 2015)
97 were fitted as rigid bodies into corresponding densities in the averaged map (Figure 1F). No clear
98 density for the Env TMD-CTD was observed in the averaged structure, even though the TMD is
99 seen in individual raw tomograms (Figure 1F), suggesting that the TMD is not strictly aligned with
100 the ectodomain or Gag-CA. The structure of the TMD-CTD (PDB ID: 6UJV) was thus placed into
101 the map based on its position relative to the Env ectodomain (Figure 1F) (Piai, Fu et al. 2020).
102 The N-terminal MA domain of immature Gag polyprotein assembles along the inner
103 membrane leaflet as a hexameric lattice of trimers (Frank, Narayan et al. 2015, Tedbury, Novikova
104 et al. 2016, Qu, Ke et al. 2021) and is connected by a flexible linker to the Gag-CA lattice
105 underneath (Tedbury and Freed 2014). Regularly spaced puncta corresponding to the Gag-MA
106 domain can be discerned directly underneath the inner leaflet and Env ectodomains in immature
107 hVLP tomograms (Figure 1F and 2A). However, distinguishable density for the Gag-MA layer
108 was not seen in the averaged immature map implying that the Gag-MA lattice (Tedbury and Freed
109 2014, Frank, Narayan et al. 2015, Tedbury, Novikova et al. 2016) may have subtle variations in
110 arrangement that deviate from Gag-CA or Env symmetry axes. Hence, based on the expected
111 position of Gag-MA relative to the Gag-CA lattice (Frank, Narayan et al. 2015, Tedbury, Novikova
112 et al. 2016), the MA lattice structure was placed into the map (Figure 1F). The resulting
113 juxtaposition of Env CTD and Gag-MA occurs right at the bottom of the inner membrane as would
114 be expected from the raw tomograms (Figures 1F and 2). From this composite model, the relative

115 position of Env CTD, when viewed normal to the membrane, is on the rim of the hexameric Gag-
116 CA lattice along its 2-fold axis (Figure 1G). This observation can also be corroborated in the raw
117 tomograms (Figure 2A and B). Thus, the trimeric Env CTD does not lie in the central hole formed
118 by the immature Gag lattice as has been hypothesized (Tedbury and Freed 2014, Tedbury,
119 Novikova et al. 2016), but instead is positioned on its hexameric rim (Figure 1G, H). In this
120 configuration, the modeled Env CTD makes direct contact with critical residues on MA that were
121 shown previously to be necessary for Env incorporation in virions (Figure 1H) (Tedbury and Freed
122 2014, Tedbury, Novikova et al. 2016).

123 To confirm that the observed Env positioning relative to Gag-CA in immature hVLPs is
124 not affected by AT-2 treatment, lack of a complete C-terminal tail or incomplete processing of
125 Gag precursor, we collected cryo-ET data of fully immature hVLPs displaying ADA.CM trimers
126 and immature VLPs displaying full-length ADA.CM trimers, without AT-2 treatment in both
127 cases. These fully immature VLPs were produced in the presence of protease inhibitor darunavir
128 such that the resulting particles have greater than 95% unprocessed Gag (Figure S4). Analysis of
129 cryo-electron tomograms from these immature VLPs having unprocessed Gag polyprotein further
130 confirmed that the organization of the Gag polyprotein, especially the MA and CA domains, is
131 similar to that seen in the AT-2 treated immature hVLPs (Figure 2). Additionally, Env trimers are
132 indeed positioned along the rim of the Gag-CA lattice and not in the central hole of the Gag-CA
133 hexamers (Figure 2D, G and H), identical to that observed in the AT-2 treated hVLP sample.
134 Preservation of this Env-Gag colocalization in the presence of truncated as well as complete
135 cytoplasmic tail suggests that a subset of CTD residues in the baseplate may be sufficient for
136 mediating interactions with Gag, but the remainder of the tail may reduce incorporation into
137 particles through steric hinderance with the Gag lattice (Buttler, Pezeshkian et al. 2018).

138 **Rearrangement of MA layer occurs during maturation**

139 In immature particles, the Gag-MA layer is consistently arrayed underneath the inner
140 membrane (Figure 1A, F and 2A, C, E, F), whereas in mature particles where the Gag polyprotein
141 has been proteolytically cleaved, the MA layer appears fragmented (Figure 2I), indicating that MA
142 rearranges during particle maturation, consistent with a recent report (Qu, Ke et al. 2021). Notably,
143 Env trimers in the mature particles are no longer colocalized with the MA layer. Given this
144 ultrastructural reorganization following maturation, it seems possible that disruption of membrane-
145 associated Gag lattices may be a prerequisite for Env trimers to gain necessary mobility to mediate
146 membrane fusion (Wyma, Jiang et al. 2004, Chojnacki, Staudt et al. 2012, Roy, Chan et al. 2013).
147 These structural changes may also provide sufficient membrane pliability for remodeling during
148 viral fusion, similar to matrix layer disruptions seen in other viruses such as influenza virus (Gui,
149 Ebner et al. 2016).

150

151 **Sub-nanometer HIV-1 Env structure shows a conformationally variable gp41 subunit**

152 A total of 32802 sub-volumes were used to reconstruct a C3-symmetric sub-tomogram
153 averaged structure of hVLP-Env with local resolution ranging between 5.7 -12 Å and a global
154 resolution of 9.1 Å (Figure 1C, 3A, B and Figure S3) (Table 1). Classification of the sub-volumes
155 did not yield any other distinct conformational class, indicating that the hVLP-Env were in a
156 predominantly closed, pre-fusion state. The Env ectodomain connects to the membrane via a thin
157 tripod stalk (Figure 1C and 3B). Though the TMD can be observed spanning the membrane layer
158 in raw tomograms (Figure 1A), no evidence of TMD is seen in the sub-tomogram averaged
159 structure (Figure 3B), similar to the Env structure from immature hVLPs.

160 Env copy number on individual mature hVLP particles ranged from 8-82 Env and the
161 trimers appeared to be randomly distributed with no apparent clustering or predisposition to
162 forming close interactions with other trimers (Figure 1B). The hVLPs have a predominantly
163 spherical morphology in our sample with an average diameter of ~100nm. Thus, by calculating
164 the surface area of the VLPs as a sphere and the Env trimer as an equilateral triangle with sides of
165 13nm length, we can determine that an average hVLP can accommodate up to 429 Env trimers
166 ($31400nm^2/73.18nm^2$) without clashing. Thus, although hVLPs display high levels of Env
167 compared to wild-type HIV, the number of surface Env trimers present on hVLPs was much lower
168 than the theoretical maximum, so Env trimers were not cramped and have sufficient surface area
169 for mobility. Furthermore, the sub-volumes used in the final reconstruction of hVLP-Env were
170 also selected to exclude neighboring Env in close proximity to avoid any influence due to unlikely
171 clashing.

172 To gain complementary structural insight into membrane embedded Env, we conducted
173 hydrogen-deuterium exchange mass-spectroscopy (HDX-MS) analysis of Env from intact hVLPs.
174 This approach samples the entire population of Env in our specimen. HDX-MS analysis showed
175 that key fiducial peptides which report on trimer integrity (Guttman and Lee 2013, Guttman,
176 Garcia et al. 2014), were well-protected in hVLP-Env (Figure 3C), confirming its closed, pre-
177 fusion conformation. Moreover, the HDX-MS spectra were unimodal, consistent with a
178 homogenous conformational population of Env. Relative to standard HDX-MS experimental
179 approaches, we were able to improve peptide coverage by performing deuterium exchanges under
180 native conditions but solubilizing the surface protein using detergent under quench conditions
181 (Figure S5). Comparison of hVLP-Env with BG505.SOSIP showed that cognate peptides
182 throughout the trimers had similar exchange profiles (Figure S6), indicating that they both have

183 comparable global conformations. However, the hVLP-Env trimer on virions exhibited greater
184 exchange protection, indicating it is in general more structurally ordered than the engineered
185 soluble trimer (Figure 3C and S6). Indeed, in terms of gp120 subunit organization, hVLP-Env has
186 a global architecture that closely resembles previously published Env structures (Kwon, Pancera
187 et al. 2015, Ward and Wilson 2015, Lee, Ozorowski et al. 2016, Pan, Peng et al. 2020). This is
188 confirmed by good agreement seen in fitting the atomic structure of detergent extracted full-length
189 Env (PDB ID: 6ULC) into the sub-tomogram averaged map (Figure 3A, B).
190

191 **Differences in gp41's terminal HR2 helix and stalk influence MPER surface exposure**

192 Significant differences relative to available structures are evident, however, in the gp41
193 subunit of hVLP-Env. In nearly all known Env structures, the HR2 helix has a long, rod-like
194 conformation with Asp664 forming its distal tip (Kwon, Pancera et al. 2015, Ward and Wilson
195 2015). In contrast, in hVLP-Env, Gln-653 forms the distal tip of the HR2 helix, making the helix
196 length 10 amino acids shorter (Figure 3B). The remaining residues in the C-terminal portion of
197 HR2 helix bend and form a thin stalk connecting the ectodomain to the membrane (Figure 3B).
198 Apart from hVLP-Env, this bend in HR2 helix has only been observed in the full-length, detergent-
199 solubilized Env structure derived from strain 92UG037.8 (Pan, Peng et al. 2020). In the presence
200 of membrane, we observe that the thin stalks, corresponding to Env residues 654-664, form a tripod
201 that elevates the ectodomain ~10 Å above the membrane (Figure 3B). As a result, the bulk of the
202 MPER (Membrane-Proximal External Region) (residues 660-683), which is a desirable vaccine
203 target of some of the most broadly neutralizing HIV-1 antibodies isolated to date (Gray, Madiga
204 et al. 2009, Rantalainen, Berndsen et al. 2020), is primarily embedded within the membrane in our
205 structure.

206 The complete MPER peptide is unresolved in all reported structures of trimeric Env, owing
207 to its membrane proximal location and/or possible variations in its conformation. Current
208 knowledge of MPER structure is only derived from constructs without the Env ectodomain
209 included (Fu, Shaik et al. 2018, Piai, Fu et al. 2020). In a recently published structure of Env from
210 BaL-1 virions, the MPER was indicated to form part of the stalk connecting Env ectodomain to
211 the membrane (Li, Li et al. 2020), which contrasts with the membrane embedded MPER location
212 identified in our structure (Figure S7). However, the embedded nature of the MPER in our map is
213 in agreement with that inferred from other solubilized full-length Env structures and biophysical
214 studies on binding of MPER-targeted antibodies to HIV-1 Env (Kim, Sun et al. 2011, Lee,
215 Ozorowski et al. 2016, Wang, Kaur et al. 2019, Rantalainen, Berndsen et al. 2020). Analyzing Env
216 structures from different HIV strains shows that the general position of the bulk of the ectodomain
217 is ~10-12 Å above the interpreted membrane surface in all cases (Figure S7). However, differences
218 arise in the position of HR2 helix and subsequent MPER sequence leading to variability in MPER
219 presentation and accessibility above the membrane amongst HIV-1 strains.
220

221 **A flexible gp41 stalk allows Env orientational freedom and MPER epitope exposure**

222 In our tomographic data, we observe tilting of hVLP-Env with respect to the membrane
223 (Figure 4A), which leads to a lower density level for the stalk in our sub-tomogram averaged map
224 (Figure 4B). Thus, the tripod stalk of Env is flexible in its membrane embedded state, allowing
225 differential sampling of MPER and other membrane-proximal epitopes. Although tilting or lifting
226 of Env from the membrane has been suggested based on bound complexes with MPER targeted
227 antibody 10E8 (Lee, Ozorowski et al. 2016, Rantalainen, Berndsen et al. 2020) and gp120-gp41

228 interface targeting antibody 35O22 (Huang, Kang et al. 2014), our results provide the first direct
229 evidence of Env tilting on native membrane in an unliganded state.

230 Sensitivity to MPER broadly neutralizing antibodies (bnAbs) has been shown to be
231 impacted by Env stability in its prefusion state (Kim, Leaman et al. 2014), with increased
232 neutralization observed after cellular receptor engagement (Frey, Peng et al. 2008, Chakrabarti,
233 Walker et al. 2011). Based on the structural data discussed above, we envision that local structure
234 of HR2, height of the Env ectodomain above membrane, and propensity of Env tilting have
235 additional impact on Env sensitivity or resistance to MPER bnAbs. To test this hypothesis, we
236 conducted comparative neutralization assays using MPER bnAbs against HIV-1 strains whose Env
237 structures have been determined. As anticipated from the structural data, amongst the three viruses,
238 ADA.CM hVLP, BaL-1 and BG505, ADA.CM was overall more resistant to MPER bnAbs (Figure
239 4C and Table S2). Neutralization and mutational analysis of proximal residues in ADA.CM that
240 contribute to trimer stability (Figure S8) showed modest individual effects but none were
241 individually responsible for ADA.CM's enhanced resistance to MPER bnAbs (Figure S8 and
242 Table S3).

243

244 **Structural variation in gp41's HR1-C helical bundle suggests a conformationally variable**
245 **central core**

246 Another prominent difference in the gp41 subunit of hVLP-Env is absence of complete
247 density in the averaged structure for the central C-terminal HR1 helices (HR1-C) (Figure 5A). The
248 HR1-C helices comprised of amino acid residues 570-595 have been a hallmark of high resolution
249 Env SOSIP structures with the central trimeric bundle composed of a HR1-C helix from each of
250 the gp41 domains. However, in our structure, only partial density for the HR1-C helix can be

251 observed corresponding to gp41 residues 570-577 and 582-595 (Figure 5A). Classification of Env
252 sub-volumes with a tight cylindrical mask for the gp41 region did not yield any subset with higher
253 density for HR1-C helices in our data. Considering that our sub-tomogram averaged map has a
254 local resolution range for the ectodomain between 5.7-12 Å (Figure S3), it is clear from
255 comparisons with other cryo-EM maps at similar resolutions, that the absence of complete HR1-
256 C helix density in our structure is not an effect of map resolution (Figure S9).

257 To ascertain whether the observed HR1-C density was affected by applied symmetry to the
258 map, we calculated an asymmetric structure of hVLP-Env at 10.7 Å resolution (Figure S3 and
259 Table 1). The asymmetric structure (Figure 5B) appears overall similar to the three-fold
260 symmetrized map (Figure 5A). Partial density for the HR1-C helices is consistently present across
261 all three protomers in the asymmetric structure, with near-complete density for HR1-C observed
262 in one protomer (Figure 5B).

263 HDX-MS analysis provides additional insight into the state of this key structural motif.
264 Peptides in HR1-C helix (residues 570-579 and 583-593) are more protected in hVLPs than in
265 BG505.SOSIP (Figure 5C), indicating increased backbone hydrogen bonding interactions in
266 corresponding residues. Taken together, the sub-tomogram averaged structures and HDX-MS
267 analysis shows that the peptides in HR1-C region exist in a stable, ordered conformation in hVLP-
268 Env even though they do not rigidly conform to Env's global three-fold structural symmetry.

269

270 **An extensive and heterogenous glycan shield in hVLP-Env protects critical epitopes**

271 The hVLP-Env structure displays distinguishable density features for N-linked glycans that
272 decorate the ectodomain surface. In contrast to most available structures where density near to
273 glycosylation sites often covers only the core GlcNAc sugars, in our unliganded hVLP-Env

274 structure, extended density for glycan moieties is observed across the protein. Resolved density
275 for multiple canonical glycan positions in gp120 and gp41 subunits extends beyond the range of
276 current structural models, revealing the extent of the 'glycan shield' (Figure 6A) (Wei, Decker et
277 al. 2003). Glycans surrounding several key bnAb epitopes can be identified in the unliganded Env
278 map, which reveal their orientations in the natural, antibody-naïve state so as to occlude underlying
279 epitopes.

280 At the CD4 receptor binding site (CD4bs) in hVLP-Env, overlaying the previously
281 determined Fab (Fragment antigen binding) structure of VRC01 (CD4bs bnAb) (Stewart-Jones,
282 Soto et al. 2016) in its binding orientation, highlights possible clashes with nearby glycans N197,
283 N276, N361 and N461 (Figure 6B). These glycans have also been shown to overlap with the
284 VRC01 epitope using molecular dynamic studies, but previously determined structures using
285 SOSIPs resolved only short glycan chains at these sites (except for N276) resulting in minimal
286 apparent glycan interactions with the bnAb (Stewart-Jones, Soto et al. 2016). In hVLP-Env,
287 extended density for these multiple glycans can be seen to clearly deter binding of CD4 epitope-
288 directed nAbs (Figure 6B). These observations are corroborated in VRC01 based neutralization
289 assays which show that hVLP-Env is substantially more resistant than BaL-1 Env (Figure 6B and
290 Table S2), whose structure lacks extended glycosylation around this site (Li, Li et al. 2020).
291 Indeed, removal of N276 and N461 glycans has been demonstrated to facilitate engagement of
292 germline precursor antibodies for VRC01-like nAbs that normally do not interact strongly with
293 natively glycosylated Env (McGuire, Hoot et al. 2013).

294 Similarly, long-range extended densities for N-linked glycans are observed in the gp120
295 domain corresponding to residues N262 and N448 as well as in the gp41 domain corresponding to
296 residues N611 and N637. The close spacing of N262/N448 to N611 likely orders these glycans to

297 be visible in the averaged map (Figure 6A, C). Collectively, these glycans form a protective barrier
298 over the fusion peptide (FP) in hVLP-Env (Figure 6C). Env's FP is essential for viral cell entry
299 but is surprisingly exposed to solution and highly dynamic by HDX-MS analysis (Figure 5C).
300 Mapping the Fab structure of FP targeting bnAb, PGT151 (Lee, Ozorowski et al. 2016), onto its
301 corresponding epitope on hVLP-Env shows how the glycans would need to be displaced in order
302 for the antibody to bind (Figure 6C). Though hVLPs are neutralized by PGT151, they are relatively
303 resistant compared to other strains (Figure 6C and Table S2), suggesting that glycan occlusion may
304 impact neutralization by FP targeted bnAbs as has been reported (Stewart-Jones, Soto et al. 2016).
305 Notably, we do not observe strong clashes with glycans at the V3-loop and V1/V2 loop
306 antibody binding super-sites. Overlaying the Fab structures of V3-loop targeting antibodies
307 PGT121 (Garces, Lee et al. 2015) and PGT128 (Lee, de Val et al. 2015), shows that the Fabs fit
308 snugly between glycans in that region, particularly N332, N136 and N301 (Figure 6D). Presence
309 of an extended N301 glycan might provide some hindrance to binding of PGT128 Fab, but we
310 only observe minimal ordered density for glycosylation at N301 in our map, which limits further
311 analysis. Similarly, when the Fab structures of V1/V2-loop targeting antibodies PG9 (Wang,
312 Gristick et al. 2017) and PGT145 (Lee, Andrabi et al. 2017) were mapped onto the sub-tomogram
313 averaged Env map, no clashes were observed with nearby glycans at positions N160 and N188
314 (Figure 6E). Antibodies to the V3-loop and V1/V2 loops, generally rely on extensive contacts with
315 neighboring glycans for their activity. As can be seen from our analysis, absence of occlusion of
316 their respective binding sites by the surrounding glycans might be an additional factor for these
317 sites to be targeted efficiently by antibodies (Andrabi, Voss et al. 2015, Moyo, Kitchin et al. 2020).
318 Extensive N-linked glycosylation densities also persist in the asymmetric structure of
319 hVLP-Env. Strikingly, we observe variations in glycan densities between different protomers,

320 indicating heterogeneity in glycan occupancy. For example, the N355 glycan is present at all three
321 protomers in the asymmetric Env reconstruction but its density varies with respect to size and
322 orientation at this site (Figure 6F). Similarly, the conserved N88 glycan, which forms part of the
323 epitope of bnAb 35O22 (Huang, Kang et al. 2014) and borders that of 10E8 (Lee, Ozorowski et
324 al. 2016), can only be observed in one protomer but not in others (Figure 6F) and is absent in the
325 C3-symmetrized map. In mass spectrometry analysis of hVLP-Env, the glycan site at N88 along
326 with several others, appear to be occupied by a heterogenous population of complex sugars (Table
327 S4). Although the observed heterogeneity in glycan processing of hVLP-Env (Table S4) is similar
328 to previous reports (Guttman, Garcia et al. 2014, Cao, Pauthner et al. 2018, Berndsen, Chakraborty
329 et al. 2020), our comparative structural analysis on asymmetric and symmetric hVLP-Env directly
330 resolves glycan heterogeneity within protomers of the same Env trimer.

331 When comparing HIV bnAbs affected by both the presence of glycan and membrane
332 proximity, binding of bnAb 35O22 (Huang, Kang et al. 2014) is highly dependent on the presence
333 of N88 glycan whereas 3BC176 binding (Lee, Leaman et al. 2015) is partially inhibited by it.
334 Mapping binding orientation of both these Fabs onto hVLP-Env results in steric clashing of the
335 Fab regions with the membrane surface (Figure 6G). Nevertheless, hVLPs are effectively
336 neutralized by 35O22 but show relative resistance to 3BC176 (Figure 6G and Table S2),
337 presumably due at least in part to 3BC176's lower binding capacity (Lee, Leaman et al. 2015).
338 Thus, a combination of the heterogenous presence of N88 glycan and tilting of hVLP-Env on the
339 membrane is consistent with the differential access of 35O22 and 3BC176 to their epitopes on
340 membrane embedded Env.

341

342

343 **Conclusions**

344 In this study, we have analyzed the structure of HIV particles displaying functional,
345 membrane-bound Env. The ADA.CM Env trimers used are highly stable in a membrane
346 environment, although they notably do not form well-ordered gp140 trimers in solution using the
347 typically employed "SOSIP" mutations (Leaman and Zwick 2013). This is true for the majority of
348 Env sequences, that require extensive stabilizing modifications in order to encourage formation of
349 stable ectodomain trimers (Rawi, Rutten et al. 2020). Thus, the structural details discussed here
350 may reflect features of Env strains that are not compatible with SOSIP modifications and thus have
351 been resistant to structural characterization so far.

352 In hVLP-Env, we find substantial evidence that key parts of gp41 including the HR1 central
353 helices and flexible stalk are not rigidly fixed relative to the rest of the trimer. Indeed, R.M.S.D.
354 calculations among static high-resolution structures of full-length Env and SOSIP structures show
355 higher deviation in the gp41 domain compared to gp120 domain (Table S5), despite the strains
356 having greater than 75% sequence similarity (Table S6). Likewise, DEER spectroscopy studies of
357 SOSIP trimers have also shown a higher degree of variability in the gp41 domain (Stadtmueller,
358 Bridges et al. 2018), further substantiating the flexible nature of gp41 as inferred from our
359 structures.

360 Our data also demonstrate that even in membrane-associated Env, the fusion peptide (FP)
361 is highly dynamic and exposed to solvent. Exposure of such a functionally critical and conserved
362 component seems counter-intuitive, but the dense clustering of glycans around the FP proximal
363 region likely confers a degree of steric protection. However, breaches in the glycan shield, revealed
364 by heterogeneity in glycan density in this region in our structures, can still offer access to the FP
365 by bnAbs (Kong, Xu et al. 2016, Lee, Ozorowski et al. 2016). Moreover, in cases where glycans

366 form part of bnAb epitopes, heterogeneity in glycosylation provide mechanisms exploited by HIV-
367 1 as a means of increasing epitope variability and facilitating evasion of antibody responses.
368 Finally, the extent of ordered density between adjacent glycans in hVLP-Env suggests that the
369 glycans are interacting in a stable manner, consistent with recent reports (Stewart-Jones, Soto et
370 al. 2016, Berndsen, Chakraborty et al. 2020).

371 By imaging Env in a membrane-bound context on VLPs, we found that, like other type I
372 fusion proteins such as SARS-CoV-2 S trimers (Ke, Oton et al. 2020), HIV-1 Env ectodomain sits
373 atop a flexible stalk that affords it considerable freedom of motion to tilt relative to the membrane.
374 This likely plays an important mechanistic role by affording fusion proteins the flexibility to bind
375 receptors and refold during membrane fusion. The flexible stalk also impacts the accessibility of
376 key epitopes that are sterically hindered on the membrane-facing side of the trimer ectodomain
377 such as the FP, gp120/gp41 interface, and membrane-associated MPER. Thus, our structural
378 analyses revealed previously uncharacterized Env features that impact presentation of prime
379 epitopes that can help explain differences in neutralization sensitivity across diverse HIV-1 strains.

380 Lastly, our structural analyses of Env in immature viral particles, shows that Env is situated
381 directly over two-fold symmetric contacts of the Gag lattice, providing the first structural evidence
382 of a direct physical Env-Gag interaction, helping to inform models for virion particle assembly
383 and Env incorporation. Taken together, our results advance understanding of HIV-1 Env in the
384 context of virion assembly, maturation and conformational sampling, revealing insights that are
385 generally unavailable through structural studies on recombinant proteins alone.

386

387

388

389 **Limitations:**

390 The ADA.CM.v4 hVLPs, which is the primary sample used in our experiments, display
391 Env that has a C-terminal truncation of 102 amino acids. This leaves about 40 amino acids of the
392 CTD on the Env protein, sufficient to form part of the baseplate revealed in a recent NMR structure
393 (Piai, Fu et al. 2020). The loss of the rest of the tail could potentially have implications in Env
394 recruitment and assembly in the VLPs. The hVLP sample was also treated with aldrithiol-2 (AT-
395 2), a mild oxidizing agent, which inactivates HIV by causing the zinc finger domain of the
396 nucleocapsid subunit to release zinc (McDonnell, De Guzman et al. 1997). However, it does not
397 act directly on the Env protein, which our data and others have showed is intact in terms of
398 structure, antigenicity, and cell receptor-mediated membrane fusion activity (Rossio, Esser et al.
399 1998, Rutebemberwa, Bess et al. 2007).

400 Our analyses of non-AT2 treated VLPs, produced in the presence of the HIV protease
401 inhibitor darunavir and displaying truncated as well as full-length Env, showed that AT-2
402 treatment did not affect direct Env interactions with the underlying Gag lattice in the immature
403 VLPs. In the mature hVLPs, the processed Gag core is not in direct contact with surface Env;
404 however, we cannot rule out an indirect effect of AT-2 on nucleocapsid and the core. Lastly, a
405 minor population of unprocessed Env (gp160 trimers) may exist, particularly on the VLPs bearing
406 full-length Env, which cannot be distinguished from mature Env (gp120-gp41 heterotrimers) at
407 the current resolution of our data. Despite the caveats above, in the range of immature particle
408 examples we have examined, Env-MA-Gag interactions remain notably consistent, thus
409 underscoring a persistent coupling between these key structural components of HIV.

410

411

Acknowledgements:

We thank the University of Washington Arnold and Mabel Beckman Cryo-EM Center and the School of Pharmacy Mass Spectrometry Center for data collection time and support. This work was supported by National Institutes of Health grants S10OD032290 and NIH NIGMS and NIAID grants R01GM099989 and R01AI140868 to K.K.L., T32 GM008268 to M.A.B., and R01AI143563 to M.B.Z., the James B. Pendleton Charitable Trust (M.B.Z.), and by the University of Washington's Proteomics Resource (UWPR95794). A grant from the Bill & Melinda Gates Foundation (OPP1126258) also supported portions of this work.

Author Contributions: V.M.P.: Conceptualization, Formal analysis, Investigation, Validation and Writing. D.P.L.: Investigation, Formal Analysis. K.N.L.: Investigation, Formal Analysis. J.T.C: Investigation, Formal Analysis. M.A.B.: Investigation. E.A.H.: Investigation. M.B.Z.: Resources, Writing review, Funding acquisition. K.K.L.: Conceptualization, Writing, Funding acquisition.

Competing interests: Authors declare no competing interests.

Data Availability: Density maps with corresponding atomic models have been deposited with accession codes EMD-XXXX, EMD-XXX, EMD-XXX, EMD-XXXX and PDB IDs XXXX and XXX.

433 **Figure Legends:**

434 **Figure 1. Structural analysis of hVLP-Env. (A)** Tomogram slice showing a mature (M) and
435 immature hVLP (IM). Blue arrows indicate Env. Orange arrow indicates Gag layer in IM with
436 zoomed inset of Gag top view on bottom right. Scale bars indicate 200 Å. Top left inset shows
437 close-up of Env with red arrows denoting TMD and yellow arrows denoting membrane bilayer.
438 (For antigenic profile of hVLPs, see Figures S1 and S2). **(B)** Representative model of mature hVLP
439 with averaged Env structure (in blue) placed onto original particle coordinates. Membrane surface
440 is shown in grey. **(C)** Sub-tomogram averaged Env structure at 9.1Å resolution (for resolution
441 related statistics, see Figure S3). OML and IML indicate outer and inner membrane leaflets,
442 respectively. **(D)** Sub-tomogram averaged Env structure from immature VLPs. OML and IML
443 indicate outer and inner membrane leaflets, respectively. **(E)** Top views of immature Gag layer
444 from relaxed C1 symmetry map (top left) and after focused refinement (top right) (see Figure S4
445 for details). Bottom panels show the same with fitted atomic structure of hexameric Gag-CA (PDB:
446 4USN). **(F)** Left: Composite model of Env-Gag structures in immature particles. Atomic
447 coordinates of Env ectodomain with Gp120 (cyan) and Gp41 (dark blue), TMD and CTD in purple
448 (PDB: 6UJV), Gag-MA hexamer (PDB: 1HIW) in green and Gag-CA hexamer in orange are
449 shown. Right: Tomogram slice of Env from an immature particle with protein components labeled.
450 Grey and green arrows indicate membrane bilayer and Gag-MA respectively. **(G)** Top view of
451 CTD (purple) and Gag-MA (green) interface. CTD lies on the rim of underlying Gag-CA hexamer
452 (orange). **(H)** Model of Env-CTD interaction with Gag-MA. Ribbon diagram of Gag-MA hexamer
453 (green) (PDB ID: 1HIW) (Hill, Worthylake et al. 1996) is shown. Residues that reduce Env
454 incorporation when mutated (13L, 17E, 31L, 35V, 99E and 75LG) are highlighted as red spheres
455 (Alfadhli, Staubus et al. 2019). Residues that reportedly suppress Env incorporation defects

456 (62QR, 35VI and 44FL) are shown as blue spheres (Alfadhli, Staubus et al. 2019). Position and
457 area covered by Env CTD structure (based on PDB ID: 6UJV (Piai, Fu et al. 2020)) in our current
458 model (left) and previously predicted models (right) is shown as purple circle. In previous models
459 (right panel), Env CTD position was predicted to be at the center of the Gag-MA hexamer. In this
460 configuration, Env CTD directly interacts with only a few residues that line the inner
461 circumference of Gag-MA hexamer. Thus, the effect of the majority of involved residues on Env
462 incorporation would be allosteric. In the current model (left panel) based on our cryo-ET data, the
463 Env CTD makes direct contacts with all Gag-MA residues determined to affect Env incorporation.
464

465 **Figure 2. HIV Env positioning over the immature Gag lattice**. **(A,B)** Representative immature
466 sub-population of AT-2 treated ADA.CM.v4 hVLP particles. **(A)** Tomogram slices through central
467 section showing position of Env (blue arrow) over MA (green arrow) and CA (orange arrow)**. (B)**
468 Top view of VLP surface plane and through Gag-CA layer. Env particles are indicated by blue
469 triangles (left panel). Right panel shows position of Env central axis (blue dot) with respect to the
470 Gag-CA hexamer (orange hexagon) when viewing along an axis perpendicular to the plane of
471 image. **(C,D)** Representative fully immature, non-AT-2 treated ADA.CM.v4 hVLP particles.
472 Tomogram slices through central section **(C)**, at VLP surface plane **(D left)** and through Gag-CA
473 layer **(D right). (E-H)** Representative fully immature, non-AT-2 treated full length ADA.CM Env
474 bearing VLP particles. Tomogram slices through central section **(E,F)** and at VLP surface plane
475 **(G, H left)** and through Gag-CA layer **(G,H right)**. Panels **D**, **G**, and **H** are all annotated in a
476 similar way as panel **B**. Notably, in all of them, Env is positioned on the rim of the Gag hexamer.
477 Black represents high density in all panels. Tomogram slice thickness is 10.32 Å in **A, B** and 8.32
478 Å in panels **C-H**. **(I)** Mature ADA.CM.v4 hVLP showing loss of Env (blue)/Gag-MA (green)

479 colocalization in cross-sectional central slice. Slice thickness is 10.32 Å. Scale bars are 200Å in
480 length.
481
482 **Figure 3. Sub-nanometer structure of hVLP-Env indicates conformational variation in HR2**
483 **helix and MPER location.** Top **(A)** and side-view **(B)** of sub-tomogram averaged Env map with
484 fitted ribbon structure adapted from full-length Env structure (PDB ID: 6ULC). Gp120 subunit is
485 colored in cyan, gp41 in dark blue, glycans are colored as red and blue heteroatoms. Outer and
486 inner membrane leaflets are indicated as OML and IML respectively. Zoomed inset shows the
487 shortened HR2 helix fitted into its respective density. Red star indicates position of Asp-664 in the
488 trimer structure (See Figure S7 for details on MPER variation). **(C)** HDX-MS of hVLP-Env shows
489 protection of peptides that report on the closed prefusion conformation of HIV-1 Env (Guttman,
490 Garcia et al. 2014, Guttman, Cupo et al. 2015) (see also Figures S5 and S6). Deuterium uptake for
491 peptides reporting on trimer integrity behave similarly between hVLP-Env and BG505.SOSIP,
492 which predominantly samples a closed prefusion conformation.
493
494 **Figure 4. Flexible gp41 stalk in HIV Env leads to variation in MPER epitope accessibility.**
495 (**A**) Top: Tomogram slices showing examples of tilted Env on membrane surface. Scale bar equals
496 100 Å. Bottom: Surface rendering of modeled Env structure (blue) in tilted orientations on
497 membrane (grey) as seen in the tomograms. **(B)** Env density map rendered at low and high
498 thresholds, respectively, showing loss of density in the stalk region (black rectangle). **(C)**
499 Comparison of neutralization effect on different HIV-1 strains by MPER-directed bnAbs. Also see
500 Figure S8.
501

502 **Figure 5. Conformational variation in central helical bundle (HR1-C) of hVLP-Env. A)** Side-
503 view of sub-tomogram averaged Env map with fitted ribbon structure and colored similar to Figure
504 1. Zoomed inset shows fit of HR1-C helix into its respective density (See also Figure S9). **B)** Top
505 and side views of an asymmetric reconstruction of hVLP-Env with the three interfaces (I1, I2 and
506 I3) of Env trimer shown along with magnified insets of fitted HR1-C helix. Black rectangle
507 indicate the central core of the trimer where the HR1-C helix lies. See Figure S3 for resolution-
508 related details. **C**) HDX-MS deuterium uptake plots for fusion peptide (FP) and HR1 peptides (see
509 also Figures S5 and S6). Surface rendering of Env was calculated using the fitted atomic model of
510 hVLP-Env in panel A without glycans. Full FP region is not observed in hVLP-Env structure due
511 to flexibility.
512
513 **Figure 6. Presence of an extensive glycan shield in hVLP-Env**. **(A)** Top and side view of hVLP-
514 Env with glycans rendered as orange ball-stick structures. Gp41 colored in dark blue and gp120 in
515 cyan. **(B-E and G)** Binding positions of eight bnAbs – VRC01 (dark grey), PGT151 (pink),
516 PGT128 (green), PGT121 (red), PG9 (light grey), PGT145 (purple), 35O22 (brown) and 3BC176
517 (green) mapped onto hVLP-Env surface. Gp120, gp41, glycan surfaces and membrane are colored
518 in cyan, dark blue, orange and grey respectively. Zoomed-in sub-panel outlines interaction surfaces
519 corresponding to each bnAb. Glycans in the vicinity of bnAb binding sites are labeled.
520 Neutralization of HIV-1 strains, ADA.CM.v4, BG505 and BaL in presence of bnAb are shown in
521 B, C and G. **F)** Differential glycosylation among trimer subunits in hVLP-Env represented using
522 glycans at N88 (orange circle) and N355 (purple oval). Surface rendering of C3-symmetrized map
523 on left followed by the three protomer interfaces from the C1 symmetry hVLP-Env map. Scale
524 bars equal 30 Å.

525 **Table 1**.

526 Data collection and processing parameters for cryo-ET and sub-tomogram averaging.

Data Collection Parameters:				
Magnification	58000X			
Voltage	300 kV			
Pixel size	2.58 Å/pixel			
Electron dose	64-68 $e^-/Å^2$			
Defocus Range (µm)	-2.5 to -5.0			
Total number of tilt-series	526			
Final number of tilt-series	423			
Data Processing Parameters:				
	hVLP-Env C3 symmetry (sym)	hVLP-Env C1 sym	Immature hVLP-Env C3 sym	Immature hVLP-Env C1 sym
Initial number of sub-volumes	63592	63592	1520	1520
Final number of sub-volumes	32802	29074	1051	1059
Map resolution at 0.143 FSC	9.13 Å	10.67 Å	31.35 Å	34.3 Å

527

528 **Experimental Methods:**

529 hVLP expression and purification:

530 Stable cell line expressing high levels of HIV Env, ADA.CM.v4, was described previously
531 (Stano, Leaman et al. 2017). A stable cell line expressing Env BG505 was generated using a similar
532 method, namely by transduction of HEK293T cells using a lentiviral vector
533 (pLentiIII.BG505.755*) containing the *env* gene BG505 with a stop codon at position 756.
534 Transduced cells were subjected to two rounds of sorting by FACS using fluorescently labeled
535 quaternary neutralizing antibody PGT145 and non-neutralizing CD4BS antibody b6, then gating
536 cells for PGT145^{high} b6^{low}. Env copy number on BG505 VLPs was notably lower than on
537 ADA.CM.v4 hVLPs. Additionally, BG505 VLPs were also more fragile, which precluded
538 extensive cryo-ET data collection and HDX-MS analysis.

539 To generate hVLPs, cells were transfected using Env-deficient HIV-1 backbone plasmid
540 pSG3ΔEnv (NIH ARRRP) and 25 kDa PEI (Polysciences) as a transfection reagent. Immature
541 hVLPs and full-length ADA pseudovirus were produced by adding the protease inhibitor darunavir
542 (NIH AIDS Reagent Program) to transfected cells at the same time as the DNA and PEI to a final
543 concentration of 2 μM. Supernatants were harvested 3 days after transfection and cleared by
544 centrifugation at 3,000 × *g* for 15 min. hVLPs were pelleted at 80,000 × *g* for 1 h and resuspended
545 100-fold concentrated in PBS. VLPs were separated from cellular debris using iodixanol density
546 gradient centrifugation. Here, concentrated hVLPs were overlaid on a 9.6 to 20.4% iodixanol
547 (Optiprep; Sigma) gradient, formed by layering iodixanol in 1.2% increments, and centrifuged at
548 200,000 × *g* for 1.5 h at 4°C in an SW41Ti rotor (Beckman). Fractions (1 ml each) were collected
549 starting from the top and fractions 6-9 were saved and pooled. Purified hVLPs were brought up to
550 15 ml with PBS and concentrated to ~0.2 ml using a 100 kDa MWCO Amicon centrifugal filter

551 (Millipore). VLPs were inactivated by adding aldrithiol-2 (AT-2) to a final concentration of 2.5
552 mM and samples were incubated at RT for 2 h. The volume was again increased to 15 ml with
553 PBS and hVLPs were concentrated using a 100 kDa MWCO centrifugal filter to 250-fold the
554 concentration in the original transfection supernatant.
555
556 Cryo-ET sample preparation and tilt-series acquisition:
557 Purified AT-2 treated hVLP samples were mixed with 10nm gold beads (Aurion BSA Gold
558 Tracer 10nm) at a ratio of 15:1 (v/v). Using a Vitrobot Mark IV (FEI Co.), 3 µl of this mixture was
559 applied to glow discharged, C-Flat 1.2/1.3, 200mesh or 400mesh grids (Electron Microscopy
560 Sciences), blotted for 4-5 seconds and plunge frozen in liquid ethane. For the non-AT-2 treated
561 immature ADA.CM VLPs and immature full-length ADA VLPs, purified sample was mixed with
562 10nm gold beads at a ratio of 10:1; 3 ul of this mixture was applied to glow-discharged 400 mesh
563 Cu Quantifoil R 1.2/1.3 grids (Electron microscopy sciences) and plunge frozen in liquid ethane.
564 Vitrobot was maintained at 4°C and 100% humidity during all these experiments.
565 For the AT-2 treated hVLPs, frozen grids were imaged using a 300 kV Titan Krios with a
566 Gatan K2 direct electron detector and GIF energy filter with slit width of 20 eV. Tilt-series were
567 collected in a dose-symmetric tilting scheme from -54° to +54° or from -48° to +48° with a step
568 size of 3° using Leginon (Carragher, Kisseberth et al. 2000) or SerialEM softwares (Mastronarde
569 2005). Tilt-series were collected in counting mode at a magnification of 53000X, corresponding
570 to a pixel size of 2.58 Å per pixel. The total dose per tilt series was ~64-68 $e^-/Å^2$. A total of 526
571 tilt-series were collected across multiple sessions.
572 For the non-AT-2 treated immature ADA.CM.v4 hVLPs and immature full-length
573 ADA.CM pseudovirus, frozen grids were imaged on a 300 kV Titan Krios equipped with a Gatan

574 K3 direct electron detector and a GIF energy filter with a slit width of 20 eV. Tilt series were
575 collected from -60° to +60° with a step size of 3° using SerialEM (Mastronarde 2005). A dose-
576 symmetric tilt scheme was applied between -48° and +48°, and the remaining angles were
577 collected with a bidirectional approach. Images were collected in super-resolution mode at a
578 nominal magnification of 64,000X, corresponding to a pixel size of 0.6932 Å/pixel. The total
579 cumulative dose was 94 e-/Å2. For the non-AT-2 treated immature full-length ADA.CM VLPs, a
580 total of 39 usable tilt-series were collected. For the non-AT-2 treated immature ADA.CM.v4
581 hVLPs, 52 usable tilt-series were collected.

582 For the non-AT-2 treated immature full-length ADA.CM pseudovirus, additional data was
583 also collected on a 200kV Glacios microscope with a K2-Summit direct electron detector. A total
584 of 17 tilt-series were collected with a nominal magnification of 28000X, corresponding to a pixel
585 size of 1.4975 Å/pixel. Tilt series were collected from -60° to +60° with a step size of 3° using
586 SerialEM with upto 45° in dose-symmetric tilt scheme (Mastronarde 2005). A total dose of 110 e-
587 /Å^2 was applied to each tilt-series.

588

589 <u>Tomogram reconstruction:</u>

590 For the AT-2 treated hVLP dataset, tilt-series image frames were corrected for beam-
591 induced motion using motioncor2 (Zheng, Palovcak et al. 2017). Using batch tomography via the
592 Etomo interface in IMOD software package (Kremer, Mastronarde et al. 1996, Mastronarde and
593 Held 2017), tilt-series were processed for tomogram generation using standard procedures. Tilt
594 series images were aligned using gold bead markers and aligned tilt-series were used to generate
595 a three-dimensional volume using weighted back-projection method. The final tomograms were

596 rotated, binned, and low pass–filtered for visualization. Tilt-series with non-optimal alignments
597 were discarded. In the end, 423 tilt-series were selected for further processing.
598 For immature ADA.CM VLPs and immature full-length ADA VLPs, Images were motion-
599 corrected using motioncor2 (Zheng, Palovcak et al. 2017) and tomograms were reconstructed and
600 CTF corrected in EMAN2 using default parameters (Chen, Bell et al. 2019).
601
602 Sub-tomogram averaging of hVLP-Env:
603 Initial model generation:
604 Eight tilt-series were randomly selected. CTF estimation and correction for these were done
605 using the Ctfplotter program (Xiong, Morphew et al. 2009). Tomograms were then generated for
606 these CTF-corrected tilt-series in IMOD at the unbinned pixel size (Kremer, Mastronarde et al.
607 1996, Mastronarde and Held 2017). The aligned tilt-series, reconstructed tomograms, file listing
608 the tilt angles and electron dose values were imported into Relion software suite (Scheres 2012)
609 according to its conventions (Bharat and Scheres 2016). Using the 3dmod graphical user interface
610 (Kremer, Mastronarde et al. 1996), 2067 Env particles on the surface of hVLPs were manually
611 picked. The picked particle coordinates were imported into Relion (Scheres 2012) and
612 corresponding sub-volumes extracted. These were then subjected to 3D classification with a
613 spherical mask covering small parts of the membrane using C1 and C3 symmetry with no initial
614 model provided. Both the C1 and C3 symmetry classifications resolved a 3D class that looked
615 similar to the expected structure of HIV-1 Env. The 3D class from the C3 symmetry run showing
616 clear Env density contained a total of 811 sub-volumes and was selected as initial model.
617
618 For C3-symmetrized hVLP-Env structure:

619 Tilt-series were imported into EMAN2's sub-tomogram averaging pipeline (Chen, Bell et
620 al. 2019). 1k X 1k tomograms were generated within EMAN2 using default parameters. The
621 binned tomograms were then used for semi-automated particle picking in PEET software
622 (Nicastro, Schwartz et al. 2006). Consolidated particles from the semi-automated picking were
623 further curated manually using the 3dmod interface (Kremer, Mastronarde et al. 1996) to remove
624 wrongly positioned particle points such as those that were in the membrane or on the inside of
625 VLPs. Curated particle coordinates (63592 particles) were then imported into EMAN2 through the
626 e2spt_boxer.py interface (Chen, Bell et al. 2019). CTF-estimation for all the tilt-series and
627 subsequent CTF-corrections were carried out within EMAN2. Sub-volumes were initially
628 extracted at 4xbinning corresponding to a pixel size of 10.32 Å per pixel. Sub-tomogram
629 refinement was carried using a spherical mask including Env on surface and a part of the
630 membrane. The 3D structure previously generated in Relion (Scheres 2012, Bharat and Scheres
631 2016) was used as initial model after low pass filtering to 60 Å. Sub-volumes were then re-
632 extracted at 2X binning using the particle orientations from the 4X binned refinement output. Sub-
633 tomogram refinement was repeated using the 2X binned data with a cylindrical mask covering
634 only the ectodomain and outer membrane layer. Particle orientations were locally refined within a
635 30º angular limit from the positions calculated in the 4Xbin refinement. Sub-volumes closer than
636 120 Å when measured between centers were removed. Sub-volumes with low cross-correlation
637 scores were also removed according to EMAN2's default settings. Remaining particles were then
638 re-extracted at the original, un-binned pixel size and re-refined starting from previously determined
639 orientations at 2X binning. Sub-tilt refinement in EMAN2 was then carried out using default
640 parameters following sub-tomogram refinement with un-binned sub-volumes (Chen, Bell et al.
641 2019). For sub-tilt refinement, a threshold mask was used that enclosed only the Env ectodomain

642 portion without any membrane density. The threshold mask was generated using the mask creation
643 tool in the Relion package (Scheres 2012). The final masked ectodomain map contained 32802
644 sub-volumes with a calculated resolution of 9.13 Å at 0.143 FSC cut-off value.
645
646 For asymmetric hVLP-Env map:
647 The initial sub-volumes used for generation of the asymmetric map were the same as that
648 used for the C3 symmetrized map described above. Refinement strategies were also nearly
649 identical between the two structures except the asymmetric map was generated with C1 symmetry.
650 However, the refinement and processing steps were carried out completely independent of each
651 other. The number of sub-volumes in the final C1 hVLP-Env structure was 29074 with a global
652 resolution of 10.67 Å at 0.143 FSC cut-off.
653
654 Structure of hVLP-Env and Gag layer from immature virions:
655 A total of 1520 sub-volumes from only immature virions were used to generate C3 and C1
656 symmetrized maps of membrane bound Env using 2Xbinned data in EMAN2 (Chen, Bell et al.
657 2019) by similar procedures as described above.
658 In the unmasked maps, a third density layer was observed underneath the membrane
659 bilayer. Relaxing symmetry of the C3-density map to C1, showed a more defined organization in
660 the Gag layer. Hence, a short, cylindrical mask enclosing only the Gag layer was used for local
661 refinement of the Gag layer using C1 symmetry, starting from the final refined positions derived
662 from the C3-symmetrized immature Env map. This focused refinement gave rise to a 23 Å map of
663 the Gag protein layer (0.143 FSC cut-off). The refined Gag-CA density map was fitted back into
664 the Gag-CA layer of the relaxed to C1 symmetry full Env map for further analyses.

665

666 Sub-tomogram averaged structure of BG505-Env from VLPs:

667 Purified BG505-VLPs were mixed with 10nm gold beads (Aurion BSA Gold Tracer 10nm)
668 at a ratio of 15:1 (v/v). The mixture was applied to C-Flat grids and plunge frozen using a Vitrobot
669 Mark IV (FEI Co.) similar to the procedure used for hVLPs above.

670 Frozen grids were imaged using a 300 kV Titan Krios with a Gatan K2 direct electron
671 detector and GIF energy filter with slit width of 20 eV. Tilt-series were collected in a dose-
672 symmetric tilting scheme from -54° to +54° with a step size of 3° using Leginon (Carragher,
673 Kisseberth et al. 2000) software. Tilt-series were collected in counting mode at a magnification of
674 53000X, corresponding to a pixel size of 2.58 Å per pixel. The total dose per tilt series was ~64-
675 68 $e^-/Å^2$. A total of 49 tilt-series were collected.

676 Tilt-series were imported into EMAN2's sub-tomogram averaging pipeline (Chen, Bell et
677 al. 2019). 1k X 1k tomograms were generated within EMAN2 using default parameters. Particle
678 points were picked manually in the e2spt_boxer.py interface (Chen, Bell et al. 2019). Further
679 refinement and processing steps were carried out similar to the hVLP-Env sub-tomogram
680 averaging procedures described above. Briefly, sub-volumes were initially extracted at 4xbinning
681 corresponding to a pixel size of 10.32 Å per pixel. Sub-tomogram refinement was carried using a
682 spherical mask including Env on surface and a part of the membrane. The initial model generated
683 for hVLP-Env in Relion (Scheres 2012, Bharat and Scheres 2016) was used as initial model for
684 BG505-Env also with low pass filtering to 60 Å. Sub-volumes were then re-extracted at 2X binning
685 using the particle orientations from the 4X binned refinement output. Sub-tomogram refinement
686 was repeated using the 2X binned data with a cylindrical mask covering only the ectodomain and
687 outer membrane layer. Particle orientations were locally refined, and duplicates were removed.

688 Sub-tilt refinement in EMAN2 was carried out using default parameters (Chen, Bell et al. 2019).
689 The final map contained 2773 sub-volumes with a calculated resolution of 16.7 Å at 0.143 FSC
690 cut-off value.
691
692 Model fitting and glycan modeling:
693 Full length Env structure from strain 92UG037.8 purified with detergents (PDB ID: 6ULC)
694 (Pan, Peng et al. 2020) was fitted as a rigid body into the 9.13 Å resolution hVLP-Env map. Each
695 protomer, comprising of gp120-gp41 heterodimer, was fitted individually into the map using
696 UCSF Chimera (Pettersen, Goddard et al. 2004). The unstructured loop region at the end of gp41,
697 comprising of amino acid residues 654-664, was fitted into the clearly delineated stalk density
698 using 'Flexible fitting' feature in Coot software (Emsley, Lohkamp et al. 2010). For modelling
699 glycan moieties, previously published high-resolution Env structures, PDB IDs: 5FUU and 5FYJ-
700 L, containing well-built glycan models were used as reference (Lee, Ozorowski et al. 2016,
701 Stewart-Jones, Soto et al. 2016). Appropriate glycan chains from these structures were copied into
702 corresponding glycan positions in the hVLP-Env map based on the presence of unoccupied
703 density. In regions where the unoccupied density was larger than the modeled glycan chains
704 available from the reference PDB structures, these extra densities were left un-modeled.
705 The final model of hVLP-Env, as generated above, was used for rigid body fitting into the
706 other sub-tomogram averaged maps of asymmetric hVLP-Env and immature hVLP-Env. All rigid
707 body fitting procedures were carried out using UCSF Chimera (Pettersen, Goddard et al. 2004).
708 Root mean square deviation (R.m.s.d) calculations between pairs of HIV Env structures
709 was carried out using UCSF Chimera (Pettersen, Goddard et al. 2004). Multiple sequence
710 alignments were carried out using the Clustal Omega web service (Madeira, Park et al. 2019).

711 Structure and tomographic images were generated using UCSF Chimera (Pettersen,
712 Goddard et al. 2004), ChimeraX (Pettersen, Goddard et al. 2021), IMOD's graphical user interface
713 (Kremer, Mastronarde et al. 1996) and ImageJ (Schneider, Rasband et al. 2012).
714
715 Neutralization assays:
716 ADA.CM.v4 hVLPs were prepared for neutralization assays as described above except
717 omitting the AT-2 inactivation step. Pseudotyped viruses were similarly produced by co-
718 transfection of HEK 293T cells using pSG3ΔEnv backbone plasmid and Env-complementation
719 plasmid. Serial dilutions of antibodies were added to virus and the mixture was incubated for 1 h
720 at 37°C prior to addition to TZM-bl target cells. DEAE-dextran was added to wells to a final
721 concentration of 10 µg/ml. After incubating for 72 h at 37°C, cells were lysed, Bright-Glo
722 luciferase reagent (Promega) was added, and luminescence was measured using a Synergy H1
723 microplate reader (Bio-Tek).
724
725 Virus ELISA:
726 ELISAs on directly immobilized hVLPs were performed as previously described (Tong,
727 Crooks et al. 2012). Briefly ADA.CM.v4 hVLPs (prepared as detailed above and treated with or
728 without AT-2) were immobilized on microwell plates at a 20x concentration for 2 h at 37˚C. Plates
729 were blocked with 4% non-fat dry milk (NFDM) PBS for 1 h at 37˚C, probed with serial dilutions
730 of primary antibodies and, subsequently, goat anti-human-Fcɣ-HRP secondary antibody (Jackson)
731 in PBS + 0.4% NFDM, and with washes using PBS between each step (detergent was omitted
732 from all steps). Signal was developed using One-step Ultra TMB Substrate (ThermoFisher).
733

734 Light microscope imaging of infected cells:

735 TZM-bl target cells were plated in 96-well plates (100 µl at 1 x 10^5/ml), and 24 hours later
736 an equal volume of hVLPs were overlaid on the cells. After a 72 hour incubation, cells were
737 imaged using a Evos FL light microscope (Life Technologies) and 20x objective.

738

739 BG505.SOSIP expression and purification:

740 Soluble BG505.SOSIP protein was expressed and purified as previously described
741 (Verkerke, Williams et al. 2016). Expi293F cells grown in Freestyle 293 media (Thermo
742 Scientific) were co-transfected with plasmids containing the SOSIP sequence and furin protease
743 in a 3:1 ratio using PEI MAX (Polysciences). Six to seven days post-transfection the supernatant
744 was cleared by filtration and the SOSIP purified by *Galanthus nivalis* lectin affinity, followed by
745 ion-exchange and hydrophobic interaction chromatography. Trimeric product was buffer
746 exchanged into PBS and stored at 4°C.

747

748 Hydrogen-deuterium mass-spectroscopy (HDX-MS) of ADA.CM.v4 particles and
749 BG505.SOSIPs:

750 HDX-MS using quench lysis method:

751 Frozen stocks of ADA.CM.v4 VLP containing approximately 0.5mg/mL envelope protein
752 or purified BG505.SOSIP diluted to the same concentration were buffer-exchanged into HEPES-
753 buffered saline (HBS, 10mM HEPES-KOH, pH 7.4, 150mM NaCl) using Zeba Spin columns with
754 a 7kDa MWCO (Thermo Fisher). 10µL of VLP solution was diluted with 90µL of deuterated HBS
755 (Hepes Buffer Saline, pH 7.4) for the indicated labeling time. The reaction was quenched and lysed
756 by addition of an equal volume of 0.2% formic acid, 4M guanidine hydrochloride, 0.2M TCEP

757 (tris(2-carboxyethyl)phosphine), 0.2% DDM (n-Dodecyl-B-D-maltoside), followed by 30s
758 incubation on ice. 20µL of a 300mg/mL solution of ZrO_2 beads (HybridSPE-Phospholipid)
759 (Adhikary, Deredge et al. 2017) in 0.1% formic acid was then added to the solution, followed by
760 vortexing for 30seconds on ice. The bead/protein mixture was then moved to a 0.22µm cellulose
761 acetate centrifuge filter tube (Spin-X, Corning) and spun for 30s at 13,000xG, 0°C. The flow-
762 through was transferred to a thin-wall PCR tube and frozen in liquid nitrogen. Samples were
763 thawed on ice and passed over a custom packed pepsin column (2.1 × 50 mm) kept at 15°C with a
764 flow of 0.1% trifluoroacetic acid (TFA), 2% acetonitrile (ACN) at 200 µL/min for 5 minutes.

765 Digested peptides were collected on a Waters XSelect CSH C18 XP VanGuard Cartridge,
766 130Å, 2.5 µm, 2.1 mm X 5 mm before separation on a Waters ACQUITY UPLC Peptide CSH
767 C18 Column, 130Å, 1.7 µm, 1 mm X 100 mm using a gradient of 7 to 14% B over 1 minute, 14
768 to 30% B over 12.5 minutes, and 30 to 50% B over 1 minute, followed by washing with three rapid
769 gradients between 95 and 5% B (A: 0.1% formic acid, 0.025% trifluoroacetic acid, 2% acetonitrile;
770 B: 0.1% formic acid in 100% acetonitrile). The liquid chromatography system was coupled to a
771 Waters Synapt G2-Si Q-TOF with ion mobility enabled. Source and de-solvation temperatures
772 were 70°C and 130°C respectively. The StepWave ion guide settings were tuned to prevent non-
773 uniform gas phase proton exchange in the source (Guttman, Wales et al. 2016).

774 During the separation step, a series of 250 µL injections were used to clean the pepsin
775 column: (1) Fos-choline-12 (Anaspec) in 0.1% TFA; (2) 2 M GuHCl in 0.1% TFA; (3) 10% acetic
776 acid, 10% ACN and 5% IPA (Majumdar, Manikwar et al. 2012, Hamuro and Coales 2018). After
777 each gradient, the trap column was washed with a series of 250 µL injections: (1) 10% FA; (2)
778 30% trifluoroethanol; (3) 80% MeOH; (4) 66% 2-propanol, 34% ACN; (5) 80% ACN (Fang, Rand
779 et al. 2011).

780 HDX-MS using solution digestion method:

781 Env on hVLPs was quantified by SDS-PAGE using BG505 SOSIPs as a standard. HDX-
782 MS reactions were initiated by diluting 20 uL of either hVLPs or BG505 SOSIPs with 180 uL
783 deuteration buffer (10 mM Phosphate, 150 mM NaCl, 85% D_2O (Cambridge Isotope
784 Laboratories)) to a final pH = 7.45. Samples were deuterated for 5 seconds, 60 seconds, 30 minutes,
785 or 3 hours before being diluted 1:1 with ice cold quench buffer (8 M urea, 200 mM TCEP [tris(2-
786 carboxyethyl) phosphine] and 0.2% formic acid (FA)) to a final pH of 2.5. Quenched samples were
787 digested with 30 ug/mL of porcine pepsin (Worthington Labs) under quench conditions for 5
788 minutes on ice. Labeled peptides were purified by high-speed centrifugation at 0°C (2 minutes at
789 25,000 rcf) and immediately flash frozen in liquid nitrogen. BG505 SOSIP samples were handled
790 identically to ensure consistent labeling and back exchange. Frozen samples were stored at -80°C
791 until analysis. All reactions were performed in duplicate.

792 Samples were thawed for 5 minutes on ice and manually injected into a custom built HDX
793 LC system kept at 0°C using a 500 uL sample loop. Samples were trapped on a Waters ACQUITY
794 UPLC CSH C18 VanGuard 130Å, 1.7 µm, 2.1 mm by 5 mm trap column for 7 minutes with a flow
795 of solvent A [2% acetonitrile, 0.1% FA, 0.025% trifluoroacetic acid (TFA)] at a rate of 150
796 µL/min. Peptides were resolved over a Waters ACQUITY UPLC CSH C18 130Å, 1.7 µm, 1 x 100
797 mm column using a 20 minute linear gradient of 3% to 50% solvent B (Solvent B: 100%
798 acetonitrile and 0.1% FA) and analyzed using Waters Synapt G2-Si Q-TOF as described above.
799 Following each injection, the sample loop and trap were washed as described above.

800 Deuterium uptake analysis was performed with HD-Examiner (Sierra Analytics) and HX-
801 Express v2 (10.1021/jasms.8b04435). For solution digestion experiments data was extracted using

802 CDCReader and analyzed using HXExpress V2 (Guttman, Weis et al. 2013) with binomial fitting
803 and bimodal deconvolution.

804 Internal exchange standards Pro-Pro-Pro-Ile [PPPI] and Pro-Pro-Pro-Phe [PPPF] were
805 included in each reaction to control for variations in ambient temperature during the labeling
806 reactions (10.1021/ac300535r). Back-exchange was measured by including bradykinin peptide at
807 2μg/mL in the deuterated buffer to serve as a fully deuterated control. The back-exchange level
808 ranged from 12-16% across experiments; deuterium uptake was not corrected.

809 Totally deuterated (TD) samples were prepared by collecting purified peptide eluent following
810 reverse phase LC separation of a pepsin digested undeuterated sample. Following evaporation of
811 the LC elution buffer the peptides were resuspended in HDX PBS pH 7.50 Buffer, deuterated in
812 deuteration Buffer for 1 hours at 65°C, and quenched and frozen as described above.

813 For peptide identification, un-deuterated peptides were collected from the LC system, dried
814 by speed-vac, and resuspended in 5% acetonitrile, 0.1% formic acid for re-injection on an Orbitrap
815 Fusion for MS/MS using EThcD fragmentation. Data was analyzed using Byonic (Protein Metrics)
816 and manually compared to undeuterated sample data.

817

818 <u>Peptic digest analysis:</u>

819 Peptic digest products were collected from the HDX chromatography system, dried by
820 speed-vacuum, and resuspended in aqueous buffer for nanoscale liquid chromatography (nanoLC-
821 MS) using a 90-minute linear gradient from 2-40% acetonitrile. Products were analyzed on an
822 Orbitrap Fusion mass spectrometer (ThermoFisher Scientific) using a high-energy collisional
823 dissociation (HCD) product-dependent electron-transfer/high-energy collision dissociation

824 (EThcD) method with a targeted mass list method with a targeted mass list using HexNAc,
825 HexHexNAc, and Hex2HexNAc m/z (204, 366, and 528 respectively) to trigger EThcD.
826 Glycopeptide data were visualized and processed by Byonic™ (Version 3.8, Protein Metrics Inc.)
827 using a 10 ppm precursor and 10 ppm fragment mass tolerance. Glycopeptides were searched using
828 the N-glycan 309 mammalian database in Protein Metrics PMI-Suite and scored based on the
829 assignment of correct c- and z- fragment ions. The true-positive entities were further validated by
830 the presence of glycan oxonium ions m/z at 204 (HexNAc ions) and 366 (HexNAcHex ions).
831
832
833 **Supplemental Information:** Supplemental information can be found online at ***
834
835 **References:**

836 Adhikary, S., D. J. Deredge, A. Nagarajan, L. R. Forrest, P. L. Wintrode and S. K. Singh (2017).
837 "Conformational dynamics of a neurotransmitter:sodium symporter in a lipid bilayer." Proc Natl
838 Acad Sci U S A **114**(10): E1786-E1795.

839 Alfadhli, A., A. O. Staubus, P. R. Tedbury, M. Novikova, E. O. Freed and E. Barklis (2019).
840 "Analysis of HIV-1 Matrix-Envelope Cytoplasmic Tail Interactions." J Virol **93**(21).

841 Andrabi, R., J. E. Voss, C. H. Liang, B. Briney, L. E. McCoy, C. Y. Wu, C. H. Wong, P.
842 Poignard and D. R. Burton (2015). "Identification of Common Features in Prototype Broadly
843 Neutralizing Antibodies to HIV Envelope V2 Apex to Facilitate Vaccine Design." Immunity
844 **43**(5): 959-973.

845 Berndsen, Z. T., S. Chakraborty, X. Wang, C. A. Cottrell, J. L. Torres, J. K. Diedrich, C. A.
846 López, J. R. Yates, M. J. van Gils, J. C. Paulson, S. Gnanakaran and A. B. Ward (2020).
847 "Visualization of the HIV-1 Env glycan shield across scales." Proc Natl Acad Sci U S A
848 **117**(45): 28014-28025.

849 Bharat, T. A. and S. H. Scheres (2016). "Resolving macromolecular structures from electron
850 cryo-tomography data using subtomogram averaging in RELION." Nat Protoc **11**(11): 2054-
851 2065.

852 Buttler, C. A., N. Pezeshkian, M. V. Fernandez, J. Aaron, S. Norman, E. O. Freed and S. B. van
853 Engelenburg (2018). "Single molecule fate of HIV-1 envelope reveals late-stage viral lattice
854 incorporation." Nat Commun **9**(1): 1861.

855 Cao, L., M. Pauthner, R. Andrabi, K. Rantalainen, Z. Berndsen, J. K. Diedrich, S. Menis, D. Sok,
856 R. Bastidas, S. R. Park, C. M. Delahunty, L. He, J. Guenaga, R. T. Wyatt, W. R. Schief, A. B.
857 Ward, J. R. Yates, D. R. Burton and J. C. Paulson (2018). "Differential processing of HIV
858 envelope glycans on the virus and soluble recombinant trimer." Nat Commun **9**(1): 3693.

859 Carragher, B., N. Kisseberth, D. Kriegman, R. A. Milligan, C. S. Potter, J. Pulokas and A.
860 Reilein (2000). "Leginon: an automated system for acquisition of images from vitreous ice
861 specimens." J Struct Biol **132**(1): 33-45.

862 Chakrabarti, B. K., L. M. Walker, J. F. Guenaga, A. Ghobbeh, P. Poignard, D. R. Burton and R.
863 T. Wyatt (2011). "Direct antibody access to the HIV-1 membrane-proximal external region
864 positively correlates with neutralization sensitivity." J Virol **85**(16): 8217-8226.

865 Checkley, M. A., B. G. Luttge and E. O. Freed (2011). "HIV-1 Envelope Glycoprotein
866 Biosynthesis, Trafficking, and Incorporation." J Mol Biol **410**(4): 582-608.

867 Chen, M., J. M. Bell, X. Shi, S. Y. Sun, Z. Wang and S. J. Ludtke (2019). "A complete data
868 processing workflow for cryo-ET and subtomogram averaging." Nat Methods **16**(11): 1161-
869 1168.

870 Chojnacki, J., T. Staudt, B. Glass, P. Bingen, J. Engelhardt, M. Anders, J. Schneider, B. Müller,
871 S. W. Hell and H. G. Kräusslich (2012). "Maturation-dependent HIV-1 surface protein
872 redistribution revealed by fluorescence nanoscopy." Science **338**(6106): 524-528.

873 Emsley, P., B. Lohkamp, W. G. Scott and K. Cowtan (2010). "Features and development of
874 Coot." Acta Crystallogr D Biol Crystallogr **66**(Pt 4): 486-501.

875 Fang, J., K. D. Rand, P. J. Beuning and J. R. Engen (2011). "False EX1 signatures caused by
876 sample carryover during HX MS analyses." Int J Mass Spectrom **302**(1-3): 19-25.

877 Frank, G. A., K. Narayan, J. W. Bess, G. Q. Del Prete, X. Wu, A. Moran, L. M. Hartnell, L. A.
878 Earl, J. D. Lifson and S. Subramaniam (2015). "Maturation of the HIV-1 core by a non-
879 diffusional phase transition." Nat Commun **6**: 5854.

880 Frey, G., H. Peng, S. Rits-Volloch, M. Morelli, Y. Cheng and B. Chen (2008). "A fusion-
881 intermediate state of HIV-1 gp41 targeted by broadly neutralizing antibodies." Proc Natl Acad
882 Sci U S A **105**(10): 3739-3744.

883 Fu, Q., M. M. Shaik, Y. Cai, F. Ghantous, A. Piai, H. Peng, S. Rits-Volloch, Z. Liu, S. C.
884 Harrison, M. S. Seaman, B. Chen and J. J. Chou (2018). "Structure of the membrane proximal
885 external region of HIV-1 envelope glycoprotein." Proc Natl Acad Sci U S A **115**(38): E8892-
886 E8899.

887 Garces, F., J. H. Lee, N. de Val, A. T. de la Pena, L. Kong, C. Puchades, Y. Hua, R. L. Stanfield,
888 D. R. Burton, J. P. Moore, R. W. Sanders, A. B. Ward and I. A. Wilson (2015). "Affinity
889 Maturation of a Potent Family of HIV Antibodies Is Primarily Focused on Accommodating or
890 Avoiding Glycans." Immunity **43**(6): 1053-1063.

891 Gray, E. S., M. C. Madiga, P. L. Moore, K. Mlisana, S. S. Abdool Karim, J. M. Binley, G. M.
892 Shaw, J. R. Mascola and L. Morris (2009). "Broad neutralization of human immunodeficiency
893 virus type 1 mediated by plasma antibodies against the gp41 membrane proximal external
894 region." J Virol **83**(21): 11265-11274.

895 Gui, L., J. L. Ebner, A. Mileant, J. A. Williams and K. K. Lee (2016). "Visualization and
896 Sequencing of Membrane Remodeling Leading to Influenza Virus Fusion." J Virol **90**(15): 6948-
897 6962.

898 Guttman, M., A. Cupo, J. P. Julien, R. W. Sanders, I. A. Wilson, J. P. Moore and K. K. Lee
899 (2015). "Antibody potency relates to the ability to recognize the closed, pre-fusion form of HIV
900 Env." Nat Commun **6**: 6144.

901 Guttman, M., N. K. Garcia, A. Cupo, T. Matsui, J. P. Julien, R. W. Sanders, I. A. Wilson, J. P.
902 Moore and K. K. Lee (2014). "CD4-induced activation in a soluble HIV-1 Env trimer." Structure
903 **22**(7): 974-984.

904 Guttman, M. and K. K. Lee (2013). "A functional interaction between gp41 and gp120 is
905 observed for monomeric but not oligomeric, uncleaved HIV-1 Env gp140." J Virol **87**(21):
906 11462-11475.

907 Guttman, M., T. E. Wales, D. Whittington, J. R. Engen, J. M. Brown and K. K. Lee (2016).
908 "Tuning a High Transmission Ion Guide to Prevent Gas-Phase Proton Exchange During H/D
909 Exchange MS Analysis." J Am Soc Mass Spectrom **27**(4): 662-668.

910 Guttman, M., D. D. Weis, J. R. Engen and K. K. Lee (2013). "Analysis of overlapped and noisy
911 hydrogen/deuterium exchange mass spectra." J Am Soc Mass Spectrom **24**(12): 1906-1912.

912 Hamuro, Y. and S. J. Coales (2018). "Optimization of Feasibility Stage for Hydrogen/Deuterium
913 Exchange Mass Spectrometry." J Am Soc Mass Spectrom **29**(3): 623-629.

914 Hill, C. P., D. Worthylake, D. P. Bancroft, A. M. Christensen and W. I. Sundquist (1996).
915 "Crystal structures of the trimeric human immunodeficiency virus type 1 matrix protein:
916 implications for membrane association and assembly." Proc Natl Acad Sci U S A **93**(7): 3099-
917 3104.

918 Huang, J., B. H. Kang, M. Pancera, J. H. Lee, T. Tong, Y. Feng, H. Imamichi, I. S. Georgiev, G.
919 Y. Chuang, A. Druz, N. A. Doria-Rose, L. Laub, K. Sliepen, M. J. van Gils, A. T. de la Peña, R.
920 Derking, P. J. Klasse, S. A. Migueles, R. T. Bailer, M. Alam, P. Pugach, B. F. Haynes, R. T.
921 Wyatt, R. W. Sanders, J. M. Binley, A. B. Ward, J. R. Mascola, P. D. Kwong and M. Connors
922 (2014). "Broad and potent HIV-1 neutralization by a human antibody that binds the gp41-gp120
923 interface." Nature **515**(7525): 138-142.

924 Ke, Z., J. Oton, K. Qu, M. Cortese, V. Zila, L. McKeane, T. Nakane, J. Zivanov, C. J. Neufeldt,
925 B. Cerikan, J. M. Lu, J. Peukes, X. Xiong, H. G. Kräusslich, S. H. W. Scheres, R. Bartenschlager
926 and J. A. G. Briggs (2020). "Structures and distributions of SARS-CoV-2 spike proteins on intact
927 virions." Nature **588**(7838): 498-502.

928 Kim, A. S., D. P. Leaman and M. B. Zwick (2014). "Antibody to gp41 MPER alters functional
929 properties of HIV-1 Env without complete neutralization." PLoS Pathog **10**(7): e1004271.

930 Kim, M., Z. Y. Sun, K. D. Rand, X. Shi, L. Song, Y. Cheng, A. F. Fahmy, S. Majumdar, G.
931 Ofek, Y. Yang, P. D. Kwong, J. H. Wang, J. R. Engen, G. Wagner and E. L. Reinherz (2011).
932 "Antibody mechanics on a membrane-bound HIV segment essential for GP41-targeted viral
933 neutralization." Nat Struct Mol Biol **18**(11): 1235-1243.

934 Kong, R., K. Xu, T. Zhou, P. Acharya, T. Lemmin, K. Liu, G. Ozorowski, C. Soto, J. D. Taft, R.
935 T. Bailer, E. M. Cale, L. Chen, C. W. Choi, G. Y. Chuang, N. A. Doria-Rose, A. Druz, I. S.
936 Georgiev, J. Gorman, J. Huang, M. G. Joyce, M. K. Louder, X. Ma, K. McKee, S. O'Dell, M.
937 Pancera, Y. Yang, S. C. Blanchard, W. Mothes, D. R. Burton, W. C. Koff, M. Connors, A. B.
938 Ward, P. D. Kwong and J. R. Mascola (2016). "Fusion peptide of HIV-1 as a site of vulnerability
939 to neutralizing antibody." Science **352**(6287): 828-833.

940 Kremer, J. R., D. N. Mastronarde and J. R. McIntosh (1996). "Computer visualization of three-
941 dimensional image data using IMOD." J Struct Biol **116**(1): 71-76.

942 Kwon, Y. D., M. Pancera, P. Acharya, I. S. Georgiev, E. T. Crooks, J. Gorman, M. G. Joyce, M.
943 Guttman, X. Ma, S. Narpala, C. Soto, D. S. Terry, Y. Yang, T. Zhou, G. Ahlsen, R. T. Bailer, M.
944 Chambers, G. Y. Chuang, N. A. Doria-Rose, A. Druz, M. A. Hallen, A. Harned, T. Kirys, M. K.
945 Louder, S. O'Dell, G. Ofek, K. Osawa, M. Prabhakaran, M. Sastry, G. B. Stewart-Jones, J.
946 Stuckey, P. V. Thomas, T. Tittley, C. Williams, B. Zhang, H. Zhao, Z. Zhou, B. R. Donald, L. K.
947 Lee, S. Zolla-Pazner, U. Baxa, A. Schon, E. Freire, L. Shapiro, K. K. Lee, J. Arthos, J. B.
948 Munro, S. C. Blanchard, W. Mothes, J. M. Binley, A. B. McDermott, J. R. Mascola and P. D.
949 Kwong (2015). "Crystal structure, conformational fixation and entry-related interactions of
950 mature ligand-free HIV-1 Env." Nat Struct Mol Biol **22**(7): 522-531.

951 Leaman, D. P. and M. B. Zwick (2013). "Increased functional stability and homogeneity of viral
952 envelope spikes through directed evolution." PLoS Pathog **9**(2): e1003184.

953 Lee, J. H., R. Andrabi, C. Y. Su, A. Yasmeen, J. P. Julien, L. Kong, N. C. Wu, R. McBride, D.
954 Sok, M. Pauthner, C. A. Cottrell, T. Nieusma, C. Blattner, J. C. Paulson, P. J. Klasse, I. A.
955 Wilson, D. R. Burton and A. B. Ward (2017). "A Broadly Neutralizing Antibody Targets the
956 Dynamic HIV Envelope Trimer Apex via a Long, Rigidified, and Anionic β-Hairpin Structure."
957 Immunity **46**(4): 690-702.

958 Lee, J. H., N. de Val, D. Lyumkis and A. B. Ward (2015). "Model Building and Refinement of a
959 Natively Glycosylated HIV-1 Env Protein by High-Resolution Cryoelectron Microscopy."
960 Structure **23**(10): 1943-1951.

961 Lee, J. H., D. P. Leaman, A. S. Kim, A. Torrents de la Pena, K. Sliepen, A. Yasmeen, R.
962 Derking, A. Ramos, S. W. de Taeye, G. Ozorowski, F. Klein, D. R. Burton, M. C. Nussenzweig,
963 P. Poignard, J. P. Moore, P. J. Klasse, R. W. Sanders, M. B. Zwick, I. A. Wilson and A. B. Ward
964 (2015). "Antibodies to a conformational epitope on gp41 neutralize HIV-1 by destabilizing the
965 Env spike." Nat Commun **6**: 8167.

966 Lee, J. H., G. Ozorowski and A. B. Ward (2016). "Cryo-EM structure of a native, fully
967 glycosylated, cleaved HIV-1 envelope trimer." Science **351**(6277): 1043-1048.

968 Li, Z., W. Li, M. Lu, J. Bess, C. W. Chao, J. Gorman, D. S. Terry, B. Zhang, T. Zhou, S. C.
969 Blanchard, P. D. Kwong, J. D. Lifson, W. Mothes and J. Liu (2020). "Subnanometer structures
970 of HIV-1 envelope trimers on aldrithiol-2-inactivated virus particles." Nat Struct Mol Biol **27**(8):
971 726-734.

972 Madeira, F., Y. M. Park, J. Lee, N. Buso, T. Gur, N. Madhusoodanan, P. Basutkar, A. R. N.
973 Tivey, S. C. Potter, R. D. Finn and R. Lopez (2019). "The EMBL-EBI search and sequence
974 analysis tools APIs in 2019." Nucleic Acids Res **47**(W1): W636-W641.

975 Majumdar, R., P. Manikwar, J. M. Hickey, J. Arora, C. R. Middaugh, D. B. Volkin and D. D.
976 Weis (2012). "Minimizing carry-over in an online pepsin digestion system used for the H/D
977 exchange mass spectrometric analysis of an IgG1 monoclonal antibody." J Am Soc Mass
978 Spectrom **23**(12): 2140-2148.

979 Mastronarde, D. N. (2005). "Automated electron microscope tomography using robust prediction
980 of specimen movements." J Struct Biol **152**(1): 36-51.

981 Mastronarde, D. N. and S. R. Held (2017). "Automated tilt series alignment and tomographic
982 reconstruction in IMOD." J Struct Biol **197**(2): 102-113.

983 McDonnell, N. B., R. N. De Guzman, W. G. Rice, J. A. Turpin and M. F. Summers (1997).
984 "Zinc ejection as a new rationale for the use of cystamine and related disulfide-containing
985 antiviral agents in the treatment of AIDS." J Med Chem **40**(13): 1969-1976.

986 McGuire, A. T., S. Hoot, A. M. Dreyer, A. Lippy, A. Stuart, K. W. Cohen, J. Jardine, S. Menis,
987 J. F. Scheid, A. P. West, W. R. Schief and L. Stamatatos (2013). "Engineering HIV envelope
988 protein to activate germline B cell receptors of broadly neutralizing anti-CD4 binding site
989 antibodies." J Exp Med **210**(4): 655-663.

990 Moyo, T., D. Kitchin and P. L. Moore (2020). "Targeting the N332-supersite of the HIV-1
991 envelope for vaccine design." Expert Opin Ther Targets **24**(6): 499-509.

992 Nicastro, D., C. Schwartz, J. Pierson, R. Gaudette, M. E. Porter and J. R. McIntosh (2006). "The
993 molecular architecture of axonemes revealed by cryoelectron tomography." Science **313**(5789):
994 944-948.

995 Pan, J., H. Peng, B. Chen and S. C. Harrison (2020). "Cryo-EM Structure of Full-length HIV-1
996 Env Bound With the Fab of Antibody PG16." J Mol Biol **432**(4): 1158-1168.

997 Pandey, A. and A. P. Galvani (2019). "The global burden of HIV and prospects for control."
998 Lancet HIV **6**(12): e809-e811.

999 Pettersen, E. F., T. D. Goddard, C. C. Huang, G. S. Couch, D. M. Greenblatt, E. C. Meng and T.
1000 E. Ferrin (2004). "UCSF Chimera--a visualization system for exploratory research and analysis."
1001 J Comput Chem **25**(13): 1605-1612.

1002 Pettersen, E. F., T. D. Goddard, C. C. Huang, E. C. Meng, G. S. Couch, T. I. Croll, J. H. Morris
1003 and T. E. Ferrin (2021). "UCSF ChimeraX: Structure visualization for researchers, educators,
1004 and developers." Protein Sci **30**(1): 70-82.

1005 Piai, A., Q. Fu, Y. Cai, F. Ghantous, T. Xiao, M. M. Shaik, H. Peng, S. Rits-Volloch, W. Chen,
1006 M. S. Seaman, B. Chen and J. J. Chou (2020). "Structural basis of transmembrane coupling of
1007 the HIV-1 envelope glycoprotein." Nat Commun **11**(1): 2317.

1008 Qu, K., Z. Ke, V. Zila, M. Anders-Össwein, B. Glass, F. Mücksch, R. Müller, C. Schultz, B.
1009 Müller, H. G. Kräusslich and J. A. G. Briggs (2021). "Maturation of the matrix and viral
1010 membrane of HIV-1." Science **373**(6555): 700-704.

1011 Rantalainen, K., Z. T. Berndsen, A. Antanasijevic, T. Schiffner, X. Zhang, W. H. Lee, J. L.
1012 Torres, L. Zhang, A. Irimia, J. Copps, K. H. Zhou, Y. D. Kwon, W. H. Law, C. A. Schramm, R.
1013 Verardi, S. J. Krebs, P. D. Kwong, N. A. Doria-Rose, I. A. Wilson, M. B. Zwick, J. R. Yates, W.
1014 R. Schief and A. B. Ward (2020). "HIV-1 Envelope and MPER Antibody Structures in Lipid
1015 Assemblies." Cell Rep **31**(4): 107583.

1016 Rawi, R., L. Rutten, Y. T. Lai, A. S. Olia, S. Blokland, J. Juraszek, C. H. Shen, Y. Tsybovsky, R.
1017 Verardi, Y. Yang, B. Zhang, T. Zhou, G. Y. Chuang, P. D. Kwong and J. P. M. Langedijk
1018 (2020). "Automated Design by Structure-Based Stabilization and Consensus Repair to Achieve
1019 Prefusion-Closed Envelope Trimers in a Wide Variety of HIV Strains." Cell Rep **33**(8): 108432.

1020 Rossio, J. L., M. T. Esser, K. Suryanarayana, D. K. Schneider, J. W. Bess, G. M. Vasquez, T. A.
1021 Wiltrout, E. Chertova, M. K. Grimes, Q. Sattentau, L. O. Arthur, L. E. Henderson and J. D.
1022 Lifson (1998). "Inactivation of human immunodeficiency virus type 1 infectivity with
1023 preservation of conformational and functional integrity of virion surface proteins." J Virol
1024 **72**(10): 7992-8001.

1025 Roy, N. H., J. Chan, M. Lambelé and M. Thali (2013). "Clustering and mobility of HIV-1 Env at
1026 viral assembly sites predict its propensity to induce cell-cell fusion." J Virol **87**(13): 7516-7525.

1027 Rutebemberwa, A., J. W. Bess, B. Brown, M. Arroyo, M. Eller, B. Slike, V. Polonis, F.
1028 McCutchan, J. R. Currier, D. Birx, M. Robb, M. Marovich, J. D. Lifson and J. H. Cox (2007).
1029 "Evaluation of aldrithiol-2-inactivated preparations of HIV type 1 subtypes A, B, and D as
1030 reagents to monitor T cell responses." AIDS Res Hum Retroviruses **23**(4): 532-542.

1031 Scheres, S. H. (2012). "RELION: implementation of a Bayesian approach to cryo-EM structure
1032 determination." J Struct Biol **180**(3): 519-530.

1033 Schneider, C. A., W. S. Rasband and K. W. Eliceiri (2012). "NIH Image to ImageJ: 25 years of
1034 image analysis." Nat Methods **9**(7): 671-675.

1035 Schur, F. K., W. J. Hagen, M. Rumlová, T. Ruml, B. Müller, H. G. Kräusslich and J. A. Briggs
1036 (2015). "Structure of the immature HIV-1 capsid in intact virus particles at 8.8 Å resolution."
1037 Nature **517**(7535): 505-508.

1038 Stadtmueller, B. M., M. D. Bridges, K. M. Dam, M. T. Lerch, K. E. Huey-Tubman, W. L.
1039 Hubbell and P. J. Bjorkman (2018). "DEER Spectroscopy Measurements Reveal Multiple
1040 Conformations of HIV-1 SOSIP Envelopes that Show Similarities with Envelopes on Native
1041 Virions." Immunity **49**(2): 235-246.e234.

1042 Stano, A., D. P. Leaman, A. S. Kim, L. Zhang, L. Autin, J. Ingale, S. K. Gift, J. Truong, R. T.
1043 Wyatt, A. J. Olson and M. B. Zwick (2017). "Dense Array of Spikes on HIV-1 Virion Particles."
1044 J Virol **91**(14).

1045 Stewart-Jones, G. B., C. Soto, T. Lemmin, G. Y. Chuang, A. Druz, R. Kong, P. V. Thomas, K.
1046 Wagh, T. Zhou, A. J. Behrens, T. Bylund, C. W. Choi, J. R. Davison, I. S. Georgiev, M. G.
1047 Joyce, Y. D. Kwon, M. Pancera, J. Taft, Y. Yang, B. Zhang, S. S. Shivatare, V. S. Shivatare, C.
1048 C. Lee, C. Y. Wu, C. A. Bewley, D. R. Burton, W. C. Koff, M. Connors, M. Crispin, U. Baxa, B.
1049 T. Korber, C. H. Wong, J. R. Mascola and P. D. Kwong (2016). "Trimeric HIV-1-Env Structures
1050 Define Glycan Shields from Clades A, B, and G." Cell **165**(4): 813-826.

1051 Tedbury, P. R. and E. O. Freed (2014). "The role of matrix in HIV-1 envelope glycoprotein
1052 incorporation." Trends Microbiol **22**(7): 372-378.

1053 Tedbury, P. R., M. Novikova, S. D. Ablan and E. O. Freed (2016). "Biochemical evidence of a
1054 role for matrix trimerization in HIV-1 envelope glycoprotein incorporation." Proc Natl Acad Sci
1055 U S A **113**(2): E182-190.

1056 Tong, T., E. T. Crooks, K. Osawa and J. M. Binley (2012). "HIV-1 virus-like particles bearing
1057 pure env trimers expose neutralizing epitopes but occlude nonneutralizing epitopes." J Virol
1058 **86**(7): 3574-3587.

1059 van Gils, M. J. and R. W. Sanders (2013). "Broadly neutralizing antibodies against HIV-1:
1060 templates for a vaccine." Virology **435**(1): 46-56.

1061 Verkerke, H. P., J. A. Williams, M. Guttman, C. A. Simonich, Y. Liang, M. Filipavicius, S. L.
1062 Hu, J. Overbaugh and K. K. Lee (2016). "Epitope-Independent Purification of Native-Like
1063 Envelope Trimers from Diverse HIV-1 Isolates." J Virol **90**(20): 9471-9482.

1064 Wang, H., H. B. Gristick, L. Scharf, A. P. West, R. P. Galimidi, M. S. Seaman, N. T. Freund, M.
1065 C. Nussenzweig and P. J. Bjorkman (2017). "Asymmetric recognition of HIV-1 Envelope trimer
1066 by V1V2 loop-targeting antibodies." Elife **6**.

1067 Wang, Y., P. Kaur, Z. J. Sun, M. A. Elbahnasawy, Z. Hayati, Z. S. Qiao, N. N. Bui, C. Chile, M.
1068 L. Nasr, G. Wagner, J. H. Wang, L. Song, E. L. Reinherz and M. Kim (2019). "Topological
1069 analysis of the gp41 MPER on lipid bilayers relevant to the metastable HIV-1 envelope prefusion
1070 state." Proc Natl Acad Sci U S A **116**(45): 22556-22566.

1071 Ward, A. B. and I. A. Wilson (2015). "Insights into the trimeric HIV-1 envelope glycoprotein
1072 structure." Trends Biochem Sci **40**(2): 101-107.

1073 Wei, X., J. M. Decker, S. Wang, H. Hui, J. C. Kappes, X. Wu, J. F. Salazar-Gonzalez, M. G.
1074 Salazar, J. M. Kilby, M. S. Saag, N. L. Komarova, M. A. Nowak, B. H. Hahn, P. D. Kwong and
1075 G. M. Shaw (2003). "Antibody neutralization and escape by HIV-1." Nature **422**(6929): 307-
1076 312.

1077 Wyma, D. J., J. Jiang, J. Shi, J. Zhou, J. E. Lineberger, M. D. Miller and C. Aiken (2004).
1078 "Coupling of human immunodeficiency virus type 1 fusion to virion maturation: a novel role of
1079 the gp41 cytoplasmic tail." J Virol **78**(7): 3429-3435.

1080 Xiong, Q., M. K. Morphew, C. L. Schwartz, A. H. Hoenger and D. N. Mastronarde (2009). "CTF
1081 determination and correction for low dose tomographic tilt series." J Struct Biol **168**(3): 378-387.

1082 Zheng, S. Q., E. Palovcak, J. P. Armache, K. A. Verba, Y. Cheng and D. A. Agard (2017).
1083 "MotionCor2: anisotropic correction of beam-induced motion for improved cryo-electron
1084 microscopy." Nat Methods **14**(4): 331-332.
1085

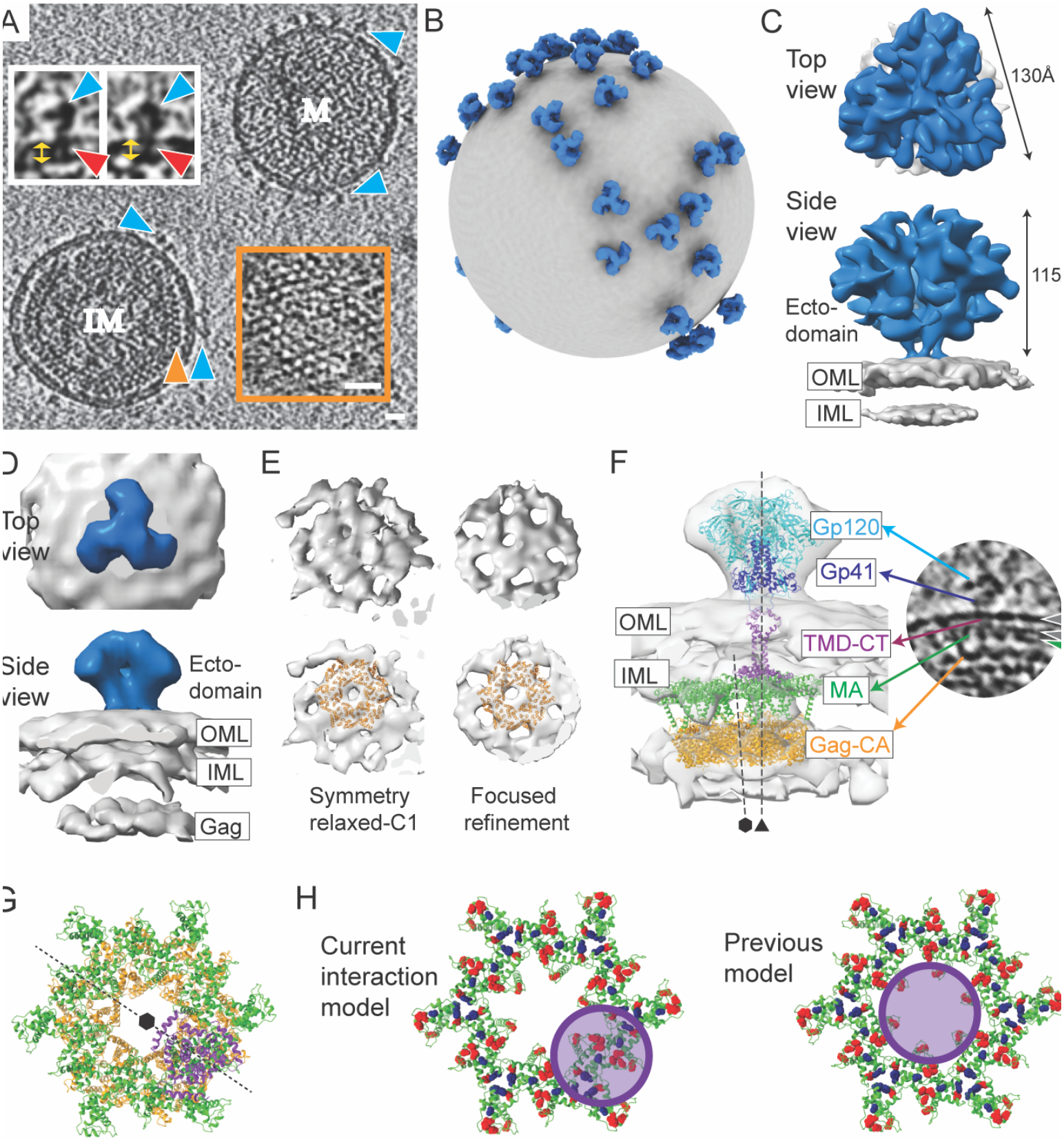
A
M
IM
B
C
Top view
130Å
Side view
115
Ecto-domain
OML
IML
D
Top view
Side view
Ecto-domain
OML
IML
Gag
E
Symmetry relaxed-C1
Focused refinement
F
Gp120
Gp41
OML
TMD-CT
IML
MA
Gag-CA
G
H
Current interaction model
Previous model

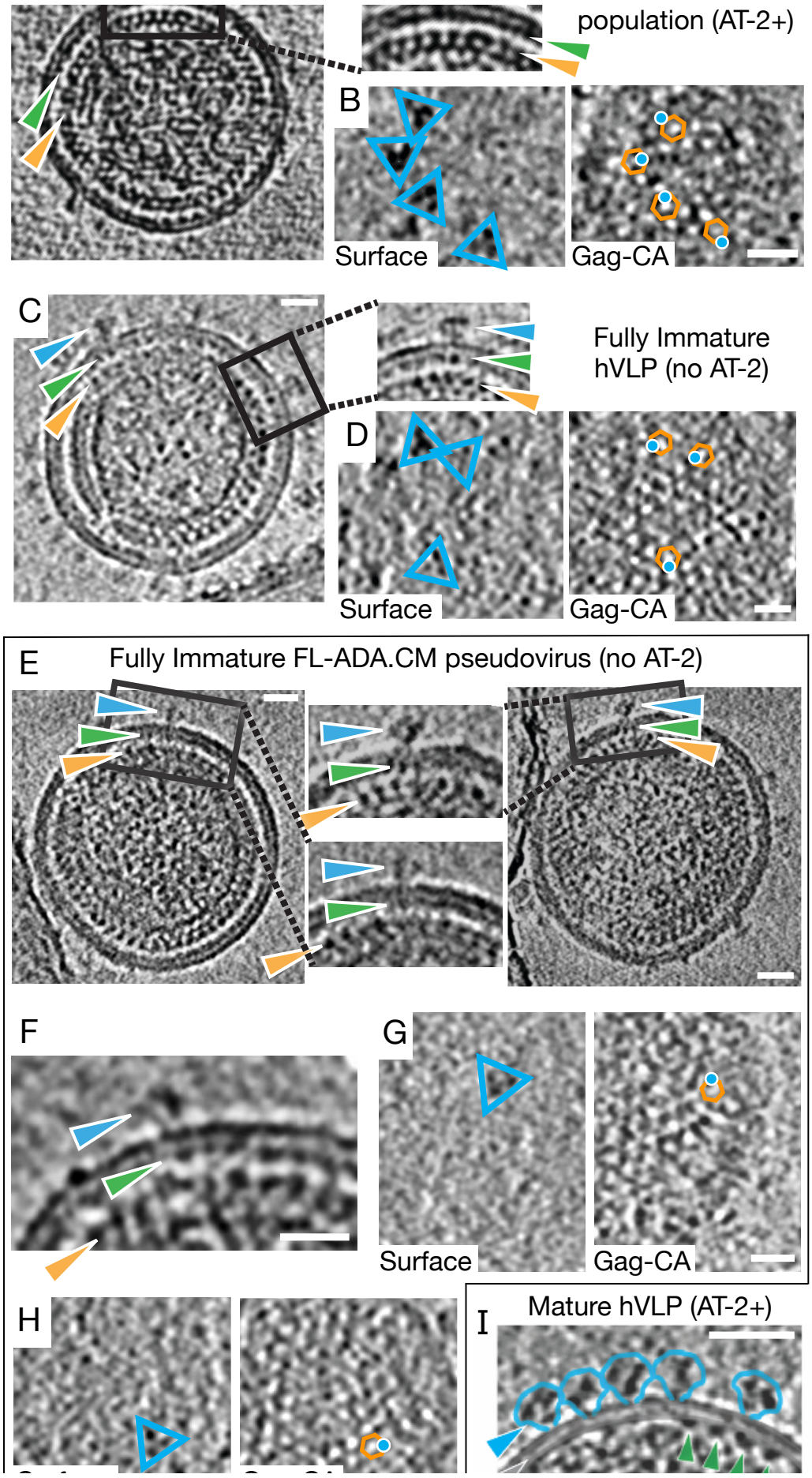
population (AT-2+)
B
Surface
Gag-CA
C
Fully Immature
hVLP (no AT-2)
D
Surface
Gag-CA
E
Fully Immature FL-ADA.CM pseudovirus (no AT-2)
F
G
Surface
Gag-CA
H
I
Mature hVLP (AT-2+)

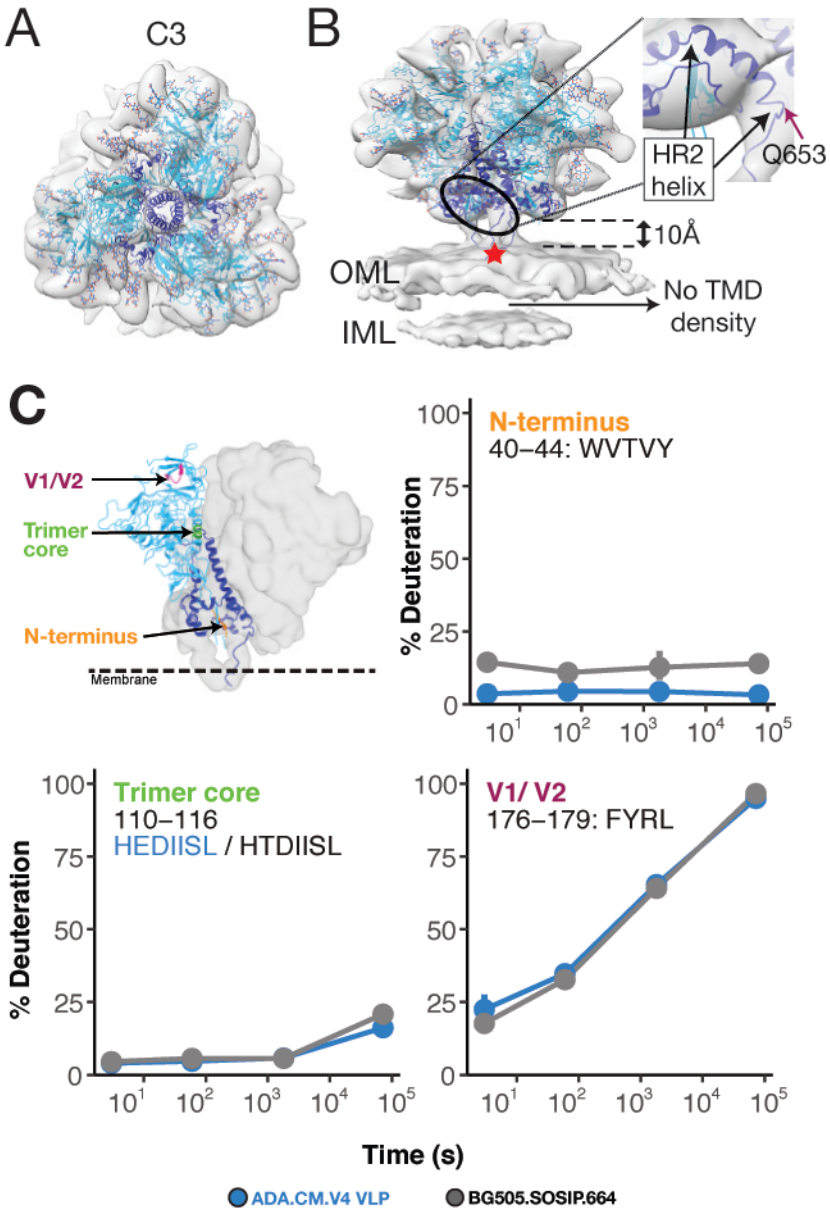
A
C3
B
HR2
helix
Q653
10Å
OML
IML
No TMD
density
C
V1/V2
Trimer
core
N-terminus
Membrane
N-terminus
40–44: WVTVY
% Deuteration
Trimer core
110–116
HEDIISL / HTDIISL
V1/ V2
176–179: FYRL
Time (s)
ADA.CM.V4 VLP
BG505.SOSIP.664

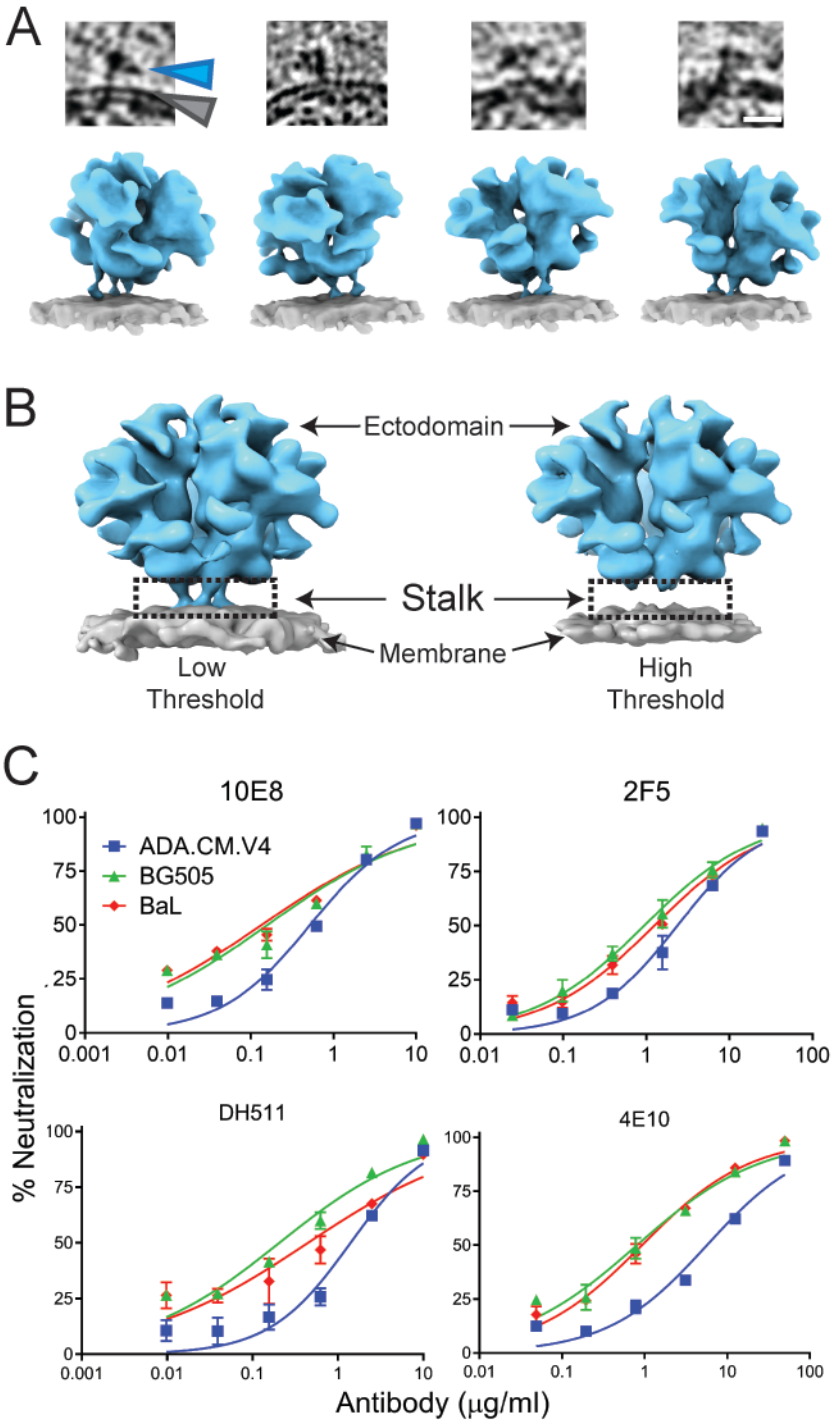
A
B
Ectodomain
Stalk
Membrane
Low
Threshold
High
Threshold
C
10E8
2F5
DH511
4E10
ADA.CM.V4
BG505
BaL
% Neutralization
Antibody (μg/ml)

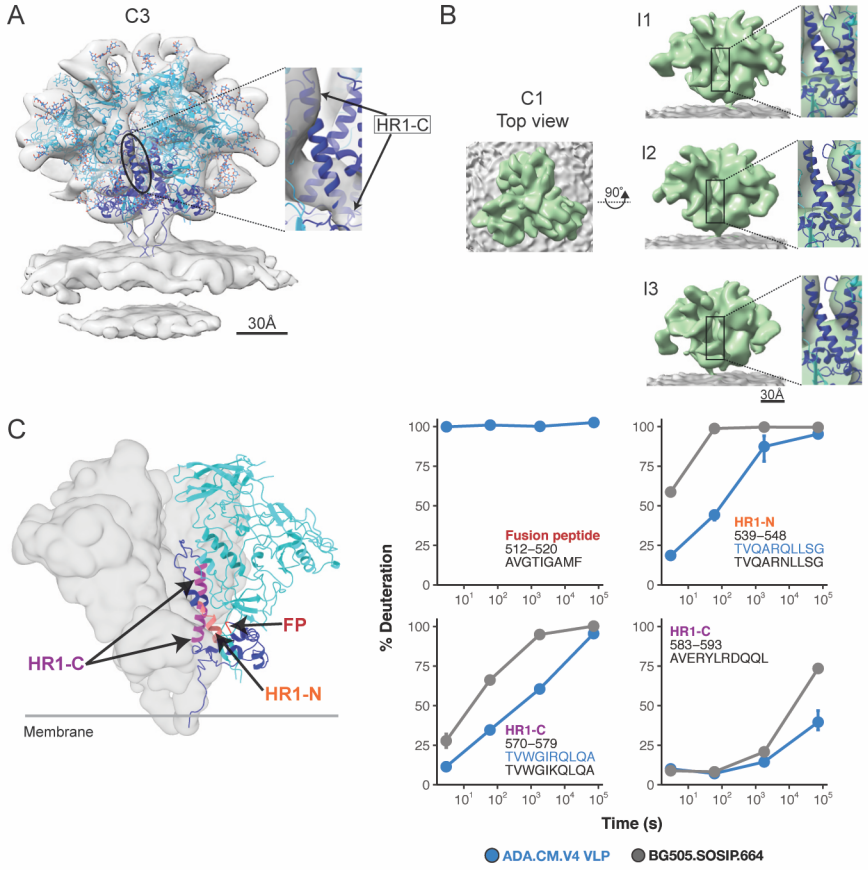
A
C3
HR1-C
30Å
B
C1
Top view
90°
I1
I2
I3
30Å
C
FP
HR1-C
HR1-N
Membrane
% Deuteration
Fusion peptide
512–520
AVGTIGAMF
HR1-N
539–548
TVQARQLLSG
TVQARNLLSG
HR1-C
570–579
TVWGIRQLQA
TVWGIKQLQA
HR1-C
583–593
AVERYLRDQQL
Time (s)
ADA.CM.V4 VLP
BG505.SOSIP.664

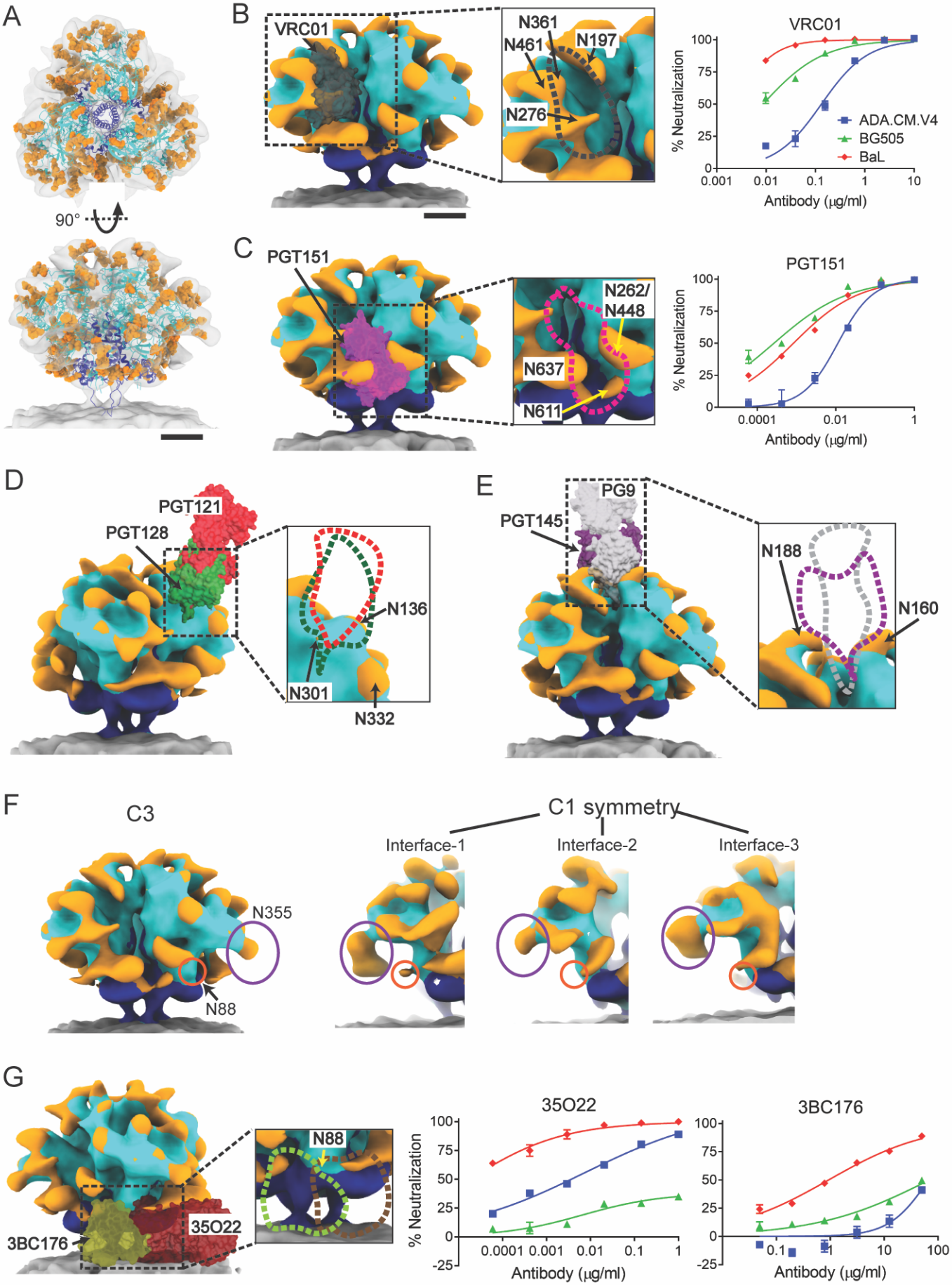
A
90°
B
VRC01
N361
N461
N197
N276
VRC01
% Neutralization
Antibody (μg/ml)
ADA.CM.V4
BG505
BaL
C
PGT151
N262/
N448
N637
N611
PGT151
% Neutralization
Antibody (μg/ml)
D
PGT121
PGT128
N136
N301
N332
E
PG9
PGT145
N188
N160
F
C3
N355
N88
C1 symmetry
Interface-1
Interface-2
Interface-3
G
N88
3BC176
35O22
35O22
% Neutralization
Antibody (μg/ml)
3BC176
Antibody (μg/ml)

Supplemental Figures:

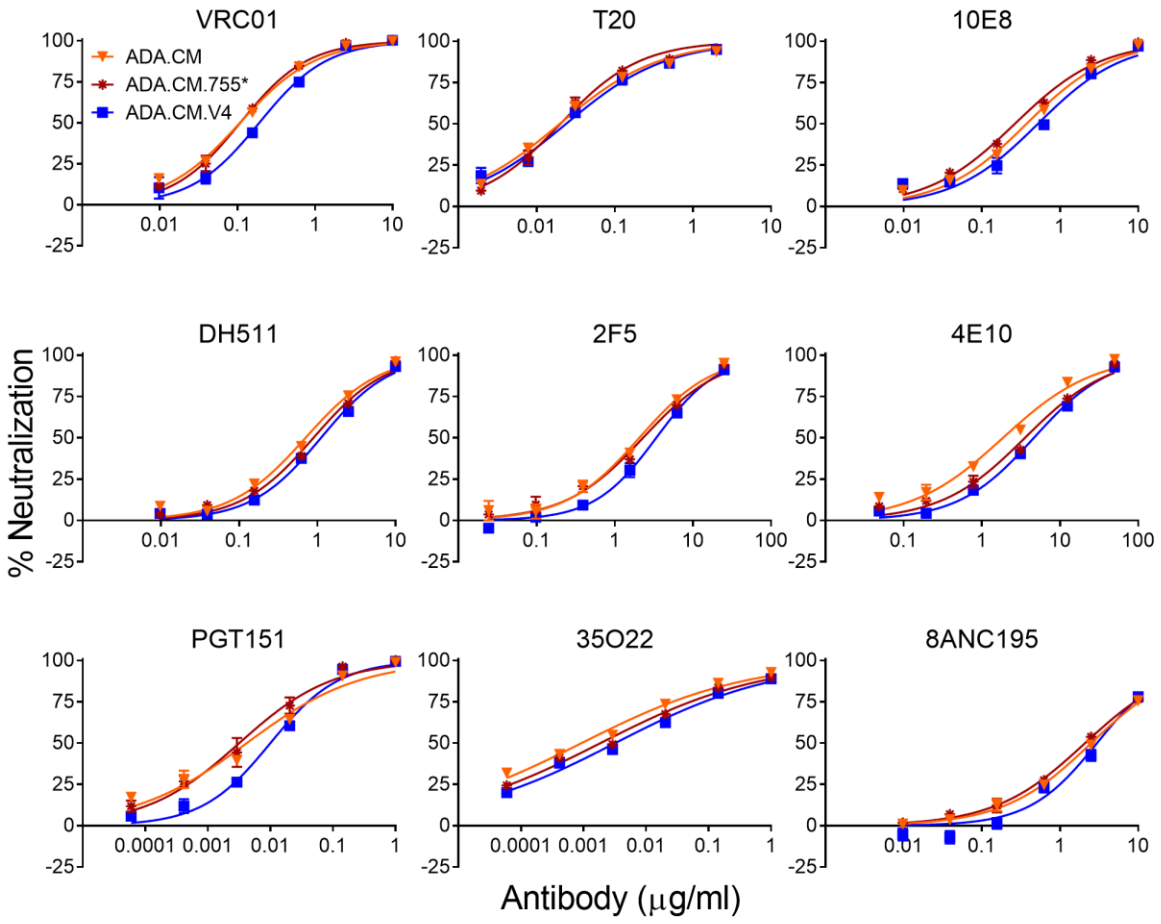

Figure S1. Percentage neutralization of HIV particles using a multi-antibody panel and the gp41 fusion inhibitor peptide, T20. Related to Figure 1.

ADA.CM and ADA.CM.755* denote pseudotyped HIV particles produced by transient transfection of HEK293T cells using a complementary two-plasmid method, with one plasmid DNA bearing the HIV backbone genes except Env, and the other plasmid bearing either Env displaying full length ADA.CM Env, or ADA.CM with a CTD truncation similar to that in hVLPs (stop codon at amino acid 756), respectively. ADA.CM.V4 refer to hVLPs produced by transient transfection of the ADA.CM.V4 high-Env HEK293T stable cell line with plasmid DNA bearing the HIV backbone genes except Env.

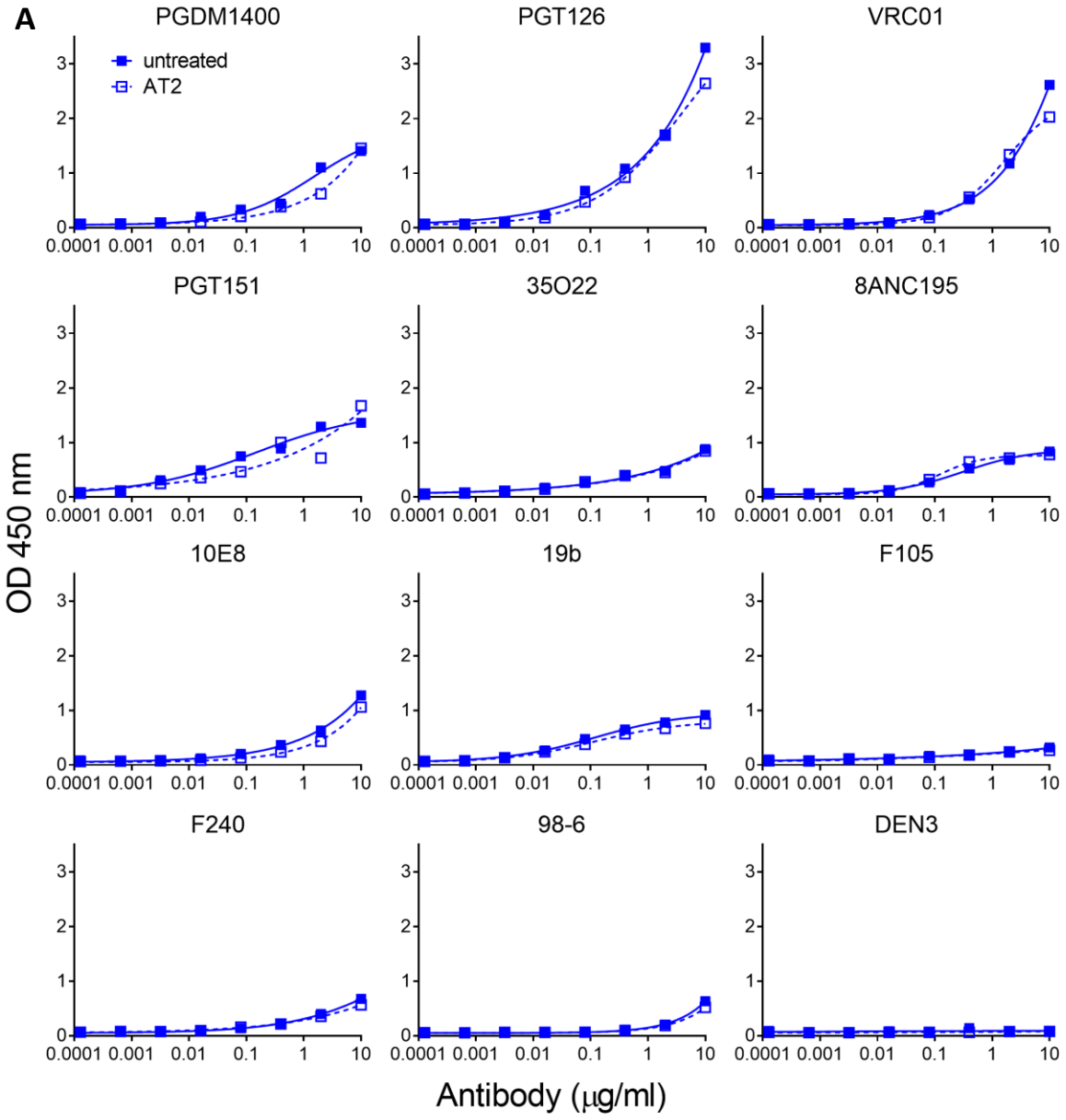
A
PGDM1400
PGT126
VRC01
untreated
AT2
PGT151
35O22
8ANC195
10E8
19b
F105
F240
98-6
DEN3
OD 450 nm
Antibody (μg/ml)
0.0001 0.001 0.01 0.1 1 10
0 1 2 3

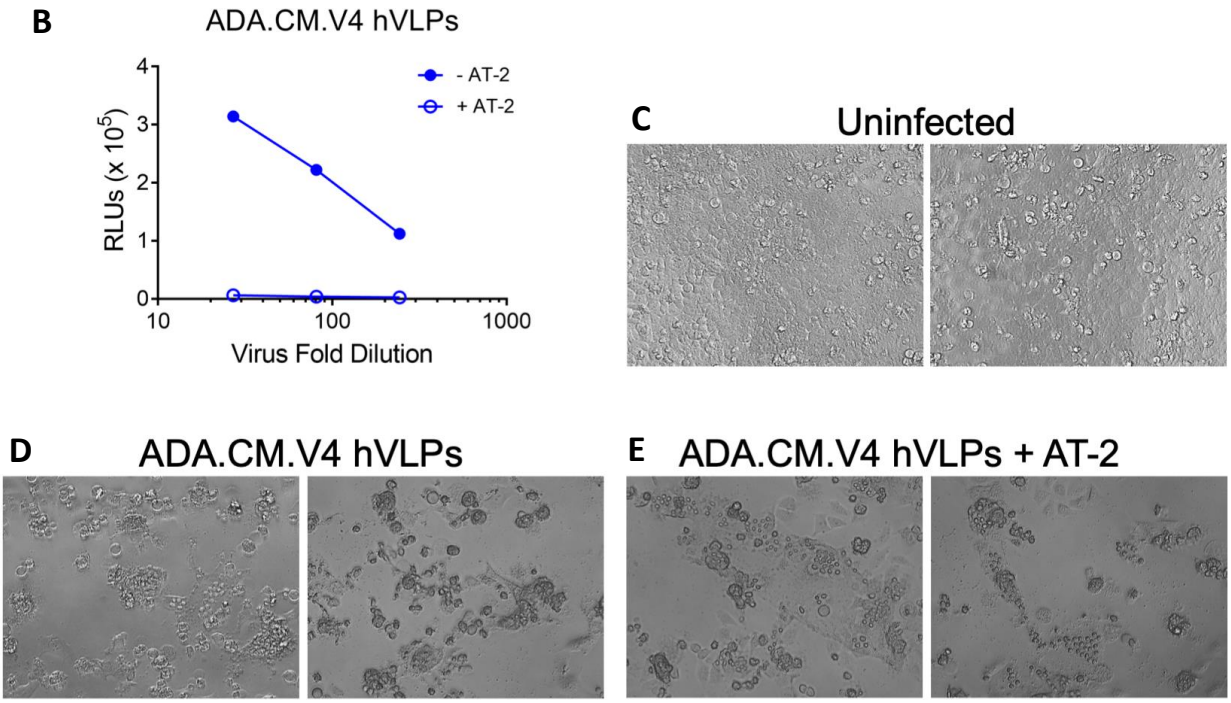

Figure S2. Effect of AT-2 treatment on hVLPs. Related to Figure 1.

(A) Binding of antibodies probed to hVLPs, as probed using an ELISA. hVLPs were treated in presence (open squares) or absence (closed squares) of AT-2 and directly immobilized on microwell plates. Binding curves show no significant difference in antibody binding on treatment with AT-2, indicating that the antigenic surface of hVLP-Env has not been altered due to AT-2 inactivation. **(B)** ADA.CM.V4 hVLPs, treated in presence (open circles) and absence (close circles) of AT-2 and normalized for p24 content, were overlaid on TZM-bl reporter cells and luciferase expression was monitored 72 hours later. AT-2-treated hVLPs do not cause productive infection. **(C-E)** Cells that had been incubated with hVLPs as in **(B)** were imaged using a light microscope and representative images are shown. Uninfected cells are monodispersed, cells incubated with hVLPs (treated either in presence or absence of AT-2) induce syncytia formation and cytotoxicity. Images are from wells in which hVLP containing supernatants were effectively diluted 3-fold prior to addition to cells.

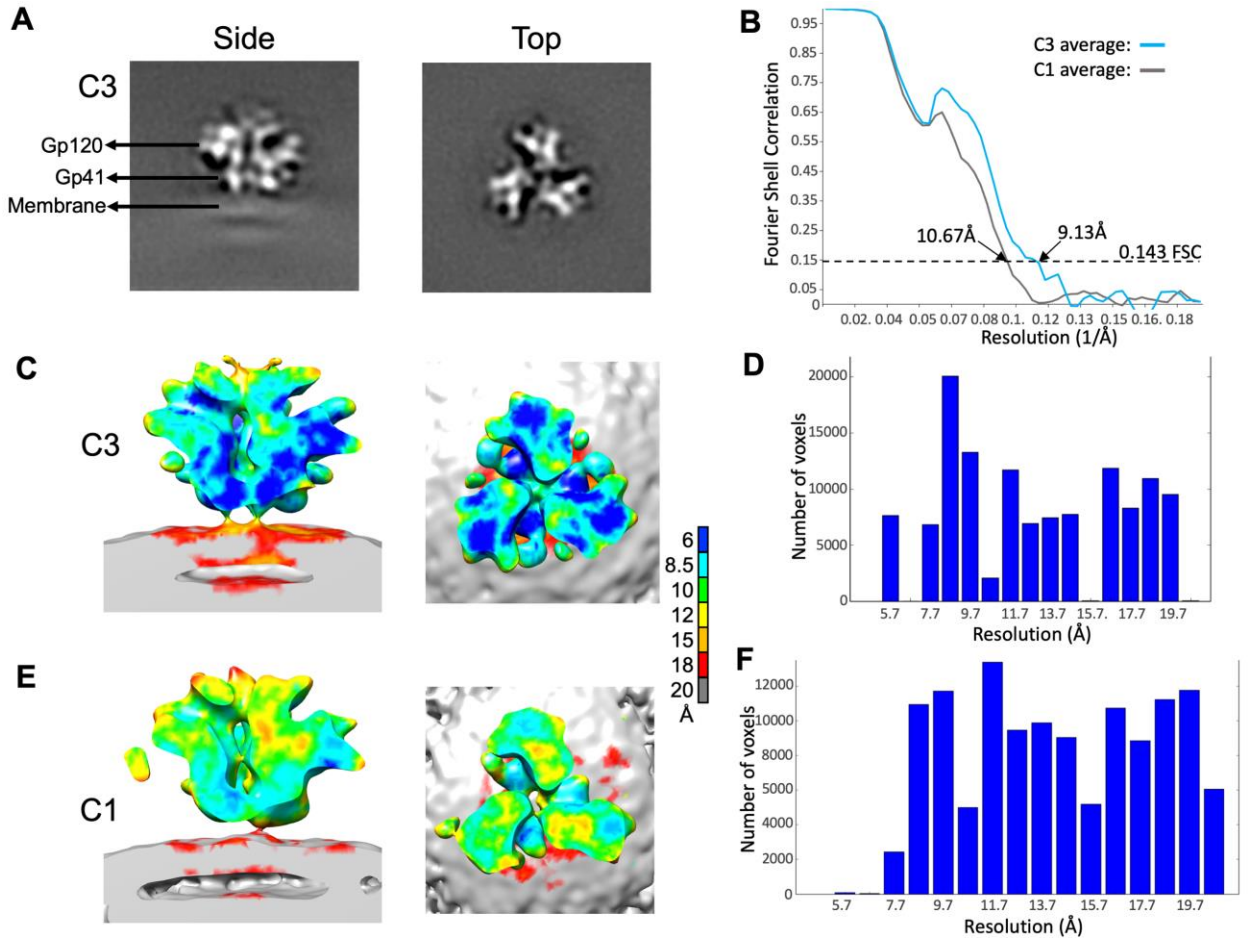

Figure S3. **Resolution estimates for hVLP-Env sub-tomogram averaged maps. Related to Figures 1, 3 and 5.**

(A) Perpendicular slices through the C3-symmetrized hVLP-Env map. **(B)** Gold-standard Fourier shell correlation (FSC) curves for C3-symmetrized map (blue line) and C1-symmetry map (grey line). Dotted line indicated the 0.143 FSC cutoff. **(C-F)** Local resolution estimation using Resmap software (Kucukelbir, Sigworth et al. 2014) for C3-symmetrized map (C,D) and asymmetric map (E,F).

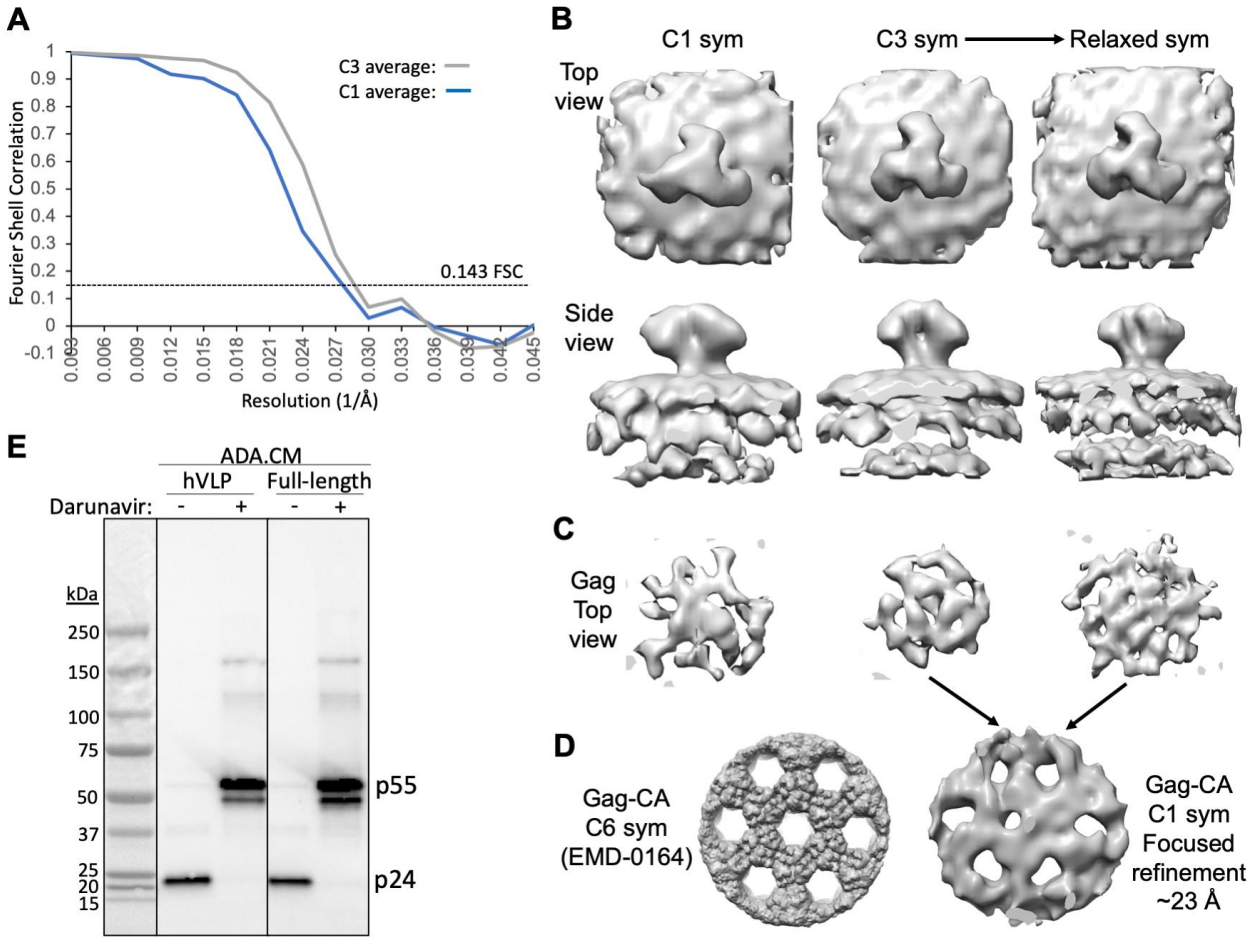

Figure S4. Structural analysis of Env, Gag-MA and Gag-CA proteins in immature hVLPs. Related to Figure 1 and 2.

(A) Fourier shell correlation (FSC) curves for C3 (grey line) and C1 (blue line) symmetrized maps of immature hVLP-Env. **(B)** Top and side surface views of immature hVLP-Env structure with C1 symmetry, C3 symmetry and the C3 map relaxed to C1 symmetry. **(C)** Top view of Gag layer from corresponding averages in panel B. **(D)** Left: Previously published high resolution density map of Gag-CA lattice, low pass filtered to ~10 Å (Mattei, Tan et al. 2018). Right: Gag-CA structure derived after focused refinement of Gag layer from the relaxed C1 symmetry immature Env map. **(E)** HIV protease inhibitor darunavir blocks the processing of immature pr55 Gag precursor into the mature p24 capsid protein. ADA.CM Env with 102 residues truncation in

CTD from hVLPs and full-length Env-CTD from pseudovirus, produced in the presence (+) or absence (-) of darunavir, were run on an SDS-PAGE gel and probed by Western blot staining with an anti-p24 antibody.

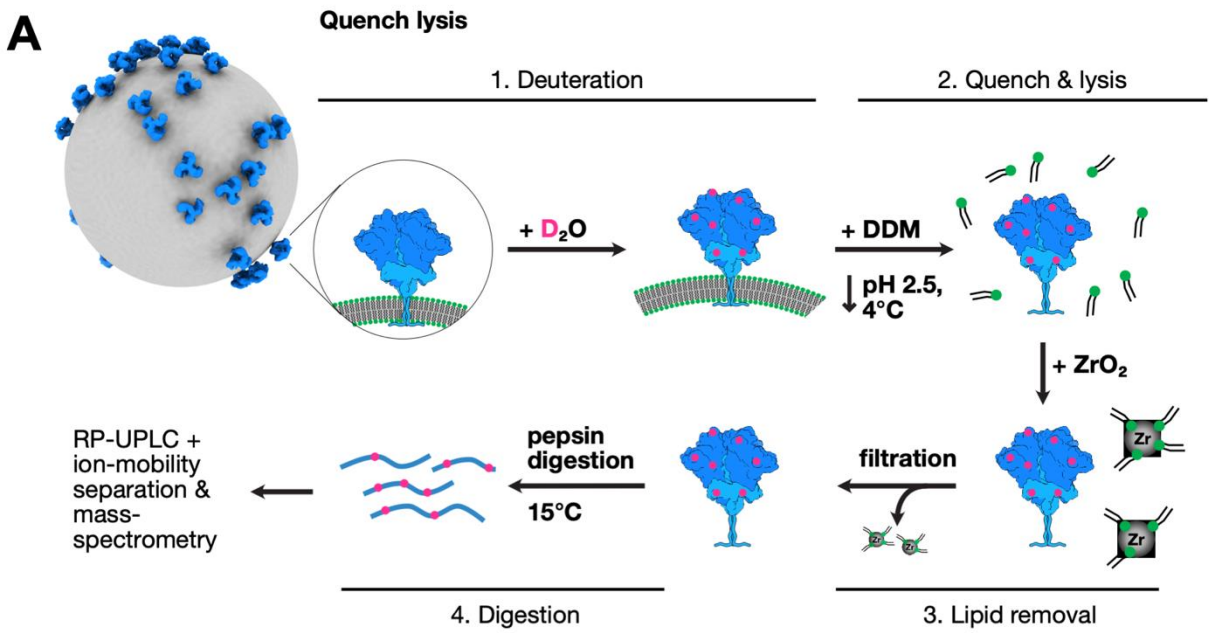
A
Quench lysis
1. Deuteration
2. Quench & lysis
+ D2O
+ DDM
pH 2.5, 4°C
+ ZrO2
Zr
filtration
pepsin digestion
15°C
RP-UPLC + ion-mobility separation & mass-spectrometry
4. Digestion
3. Lipid removal

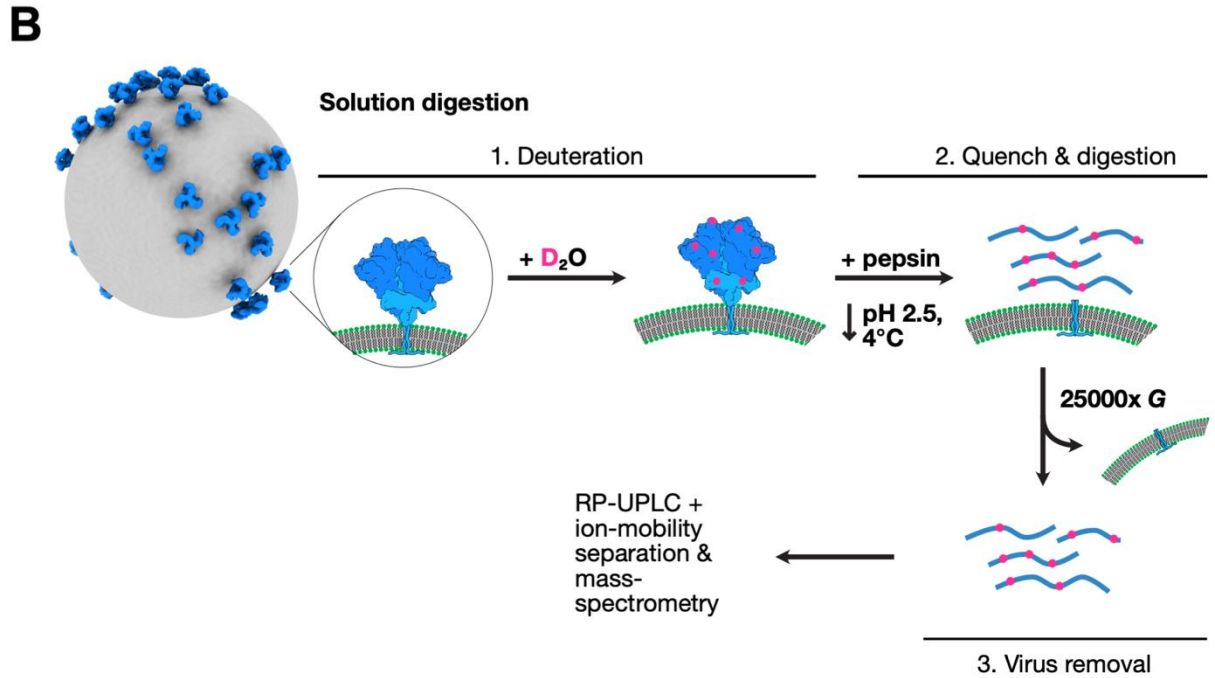
B
Solution digestion
1. Deuteration
2. Quench & digestion
+ D2O
+ pepsin
pH 2.5, 4°C
25000x G
RP-UPLC + ion-mobility separation & mass-spectrometry
3. Virus removal

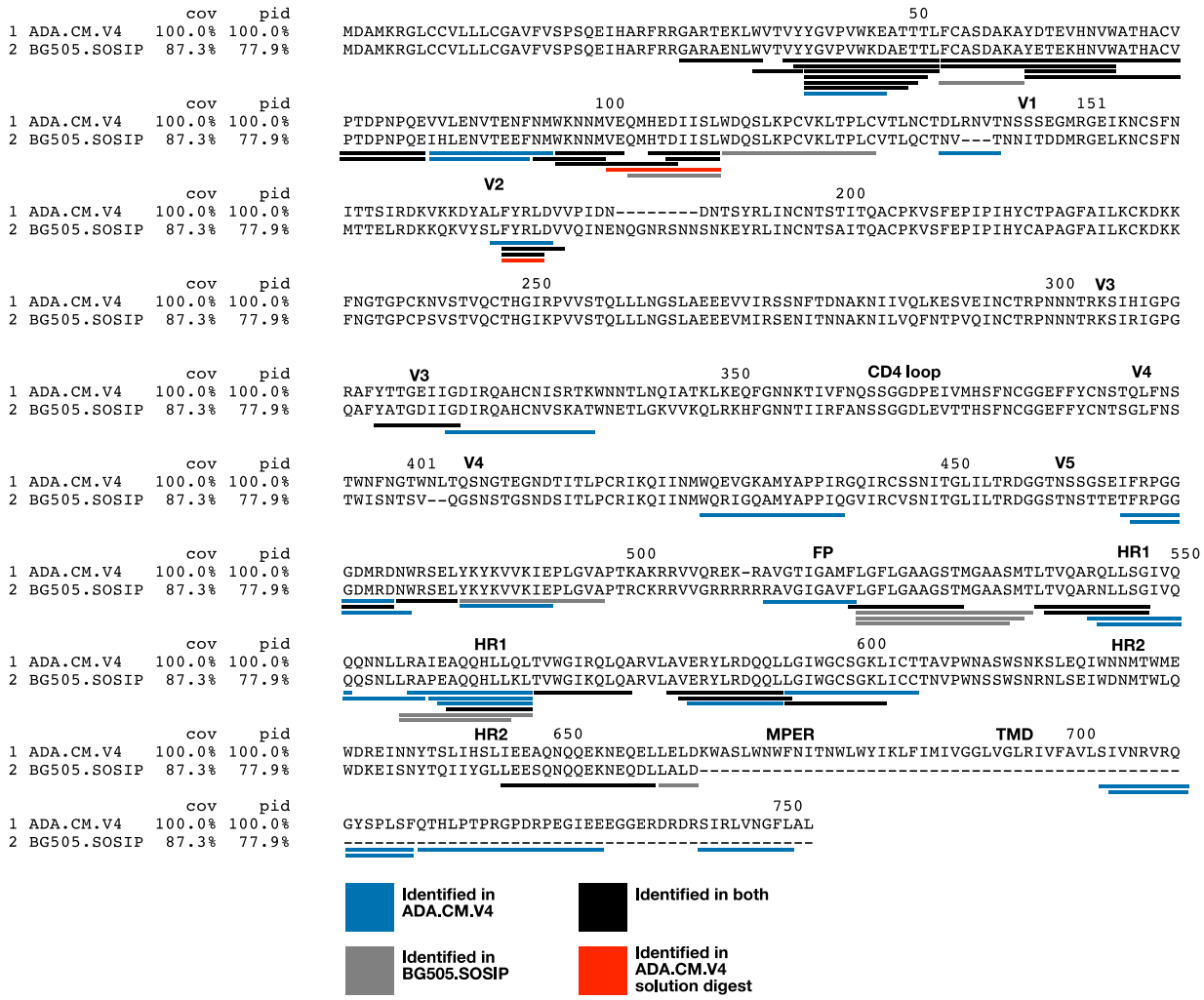

Figure S5. **Hydrogen-deuterium exchange mass spectroscopy (HDX-MS) methods used for hVLP-Env analysis. Related to Figures 3 and 5.**

(A) Quench Lysis method: Improved procedure to increase peptide coverage in HDX-MS experiment. hVLP particles were treated with deuterated water (D_2O) in native, neutral pH conditions for varying periods of time. The reaction was quenched along with detergent treatment to solubilize Env. Zirconium beads (Zr) were used to filter out the lipid molecules before downstream peptidase digestion and mass-spectrometry analysis (see Methods for details). **(B)** Solution digestion method: Routine HDX-MS procedure where after deuteration of hVLP-Env in native, neutral pH, the reaction is quenched, and peptidase treatment is carried out

with Env fixed on particle surface. **(C)** Peptide coverage map of hVLP-Env by quench lysis HDX-MS. Sequence alignment of ADA.CM and BG505.SOSIP used in the HDX-MS experiments. BG505.SOSIP includes residues only upto 664 and does not contain MPER, TMD or CTT domains. Underlined peptide regions are color coded based on their identification in the quench lysis HDX-MS experiment. Peptides underlined in red are those identified by solution digest HDX-MS. Important regions of Env such as variable loops (V1-V5), CD4 receptor binding loop, fusion peptide (FP), heptad repeat helices (HR1 and HR2), MPER and TMD are highlighted and labeled.

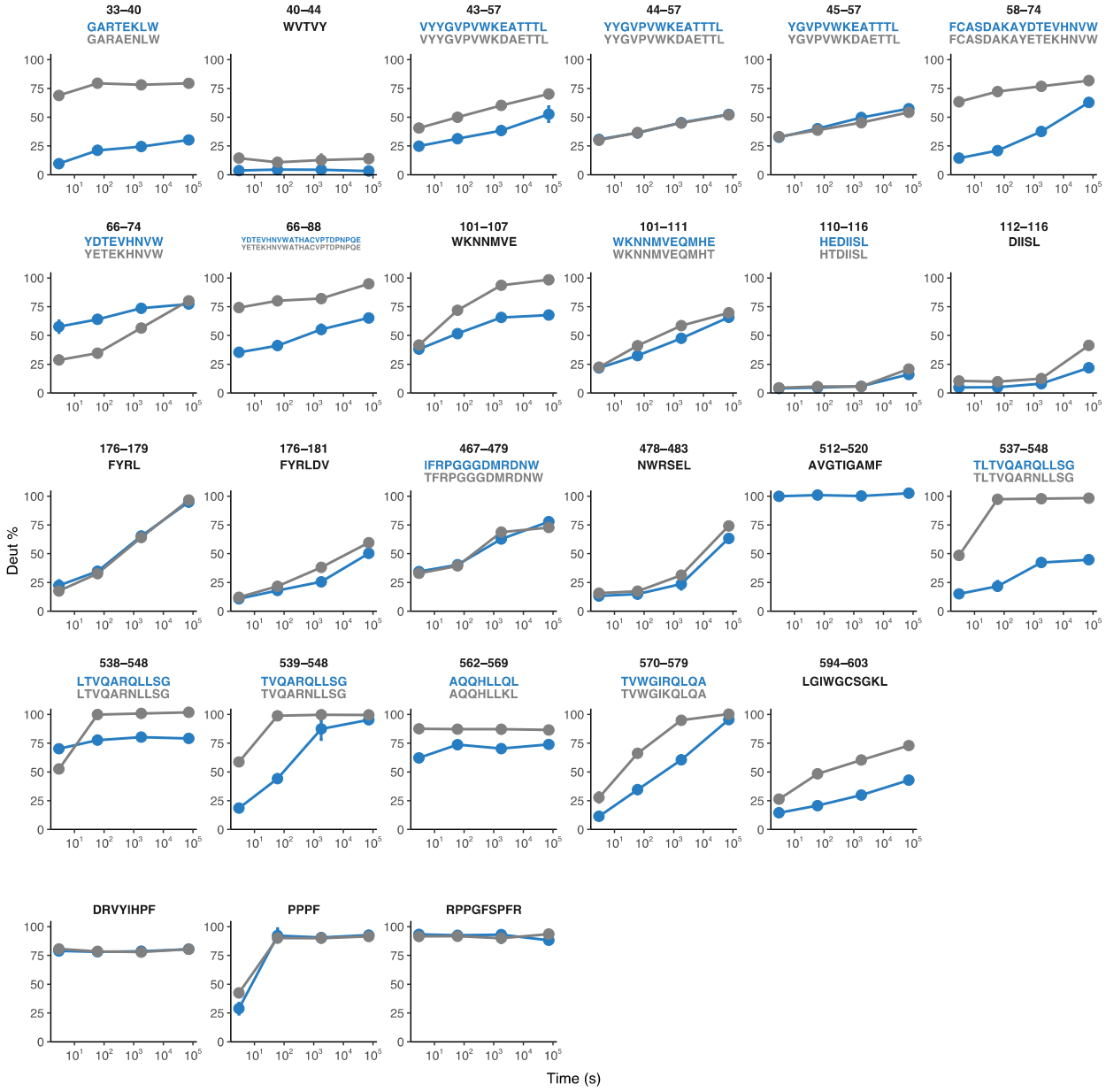

Figure S6. Deuterium uptake plots from HDX-MS experiment. Related to Figures 3 and 5. Deuterium uptake plots for all peptides in Env ectodomain commonly identified between hVLP-Env (blue) and BG505.SOSIP (grey). Corresponding sequence of the peptides are given above each uptake plot. Bottom three panels are back-exchange peptide standards (DRVYIHPF and RPPGFSPFR) and exchange rate peptide standard (PPPF). Refer to Figure S10 for sequence alignment between the two Envs.

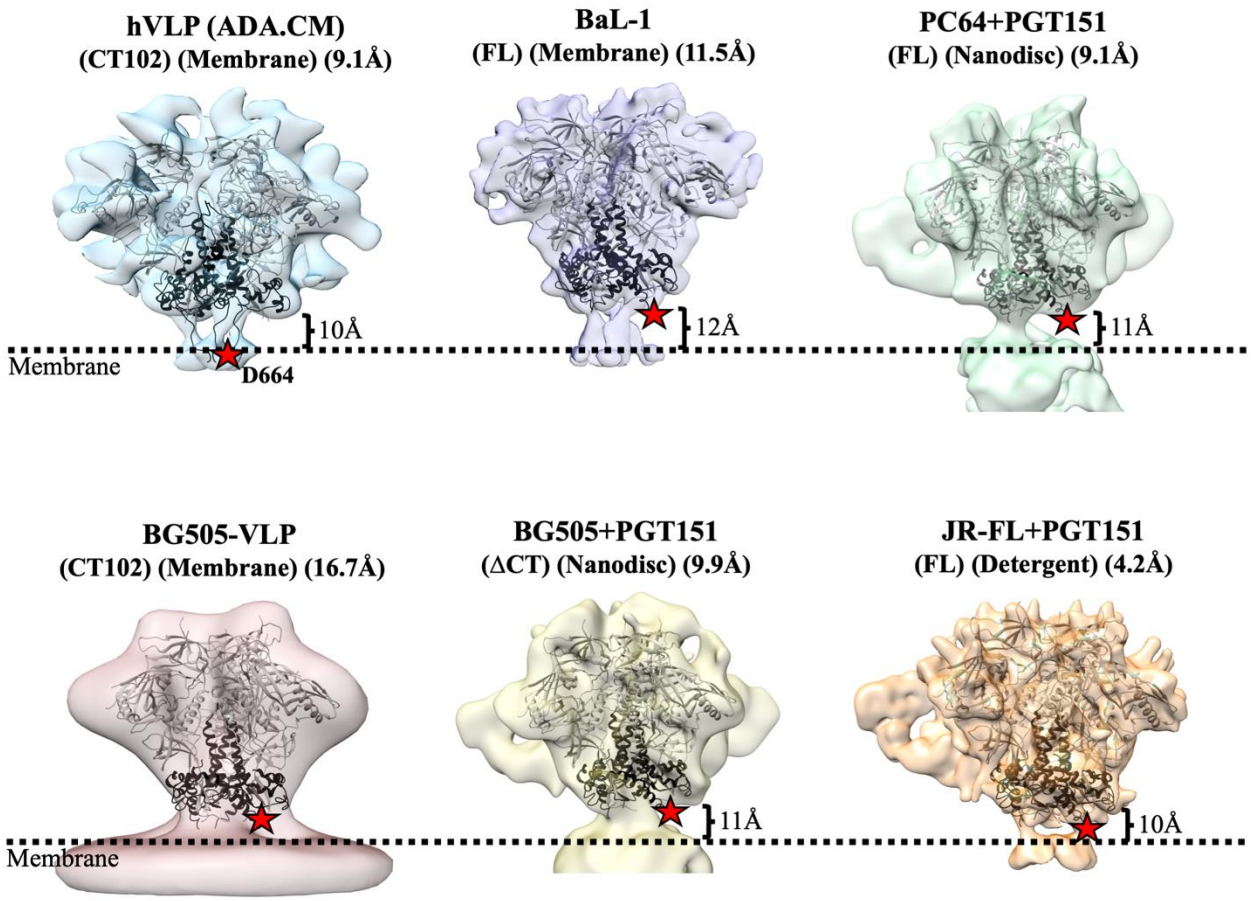

Figure S7. Position of Env ectodomain with respect to membrane surface. Related to Figure 3.

Surface view of Env structure from different HIV strains: hVLP (ADA.CM), BaL-1, PC64, BG505 and JR-FL. Position of outer membrane surface as interpreted for each of the structures is indicated by a dotted black line. Position of Asp-664, which forms the end of HR2 helix region in gp41, is denoted by a red star in all structures. Low resolution structure of near full length BG505 in native membrane was obtained from VLPs displaying high levels of BG505 Env and having a CTD truncation similar to that in hVLP-Env.

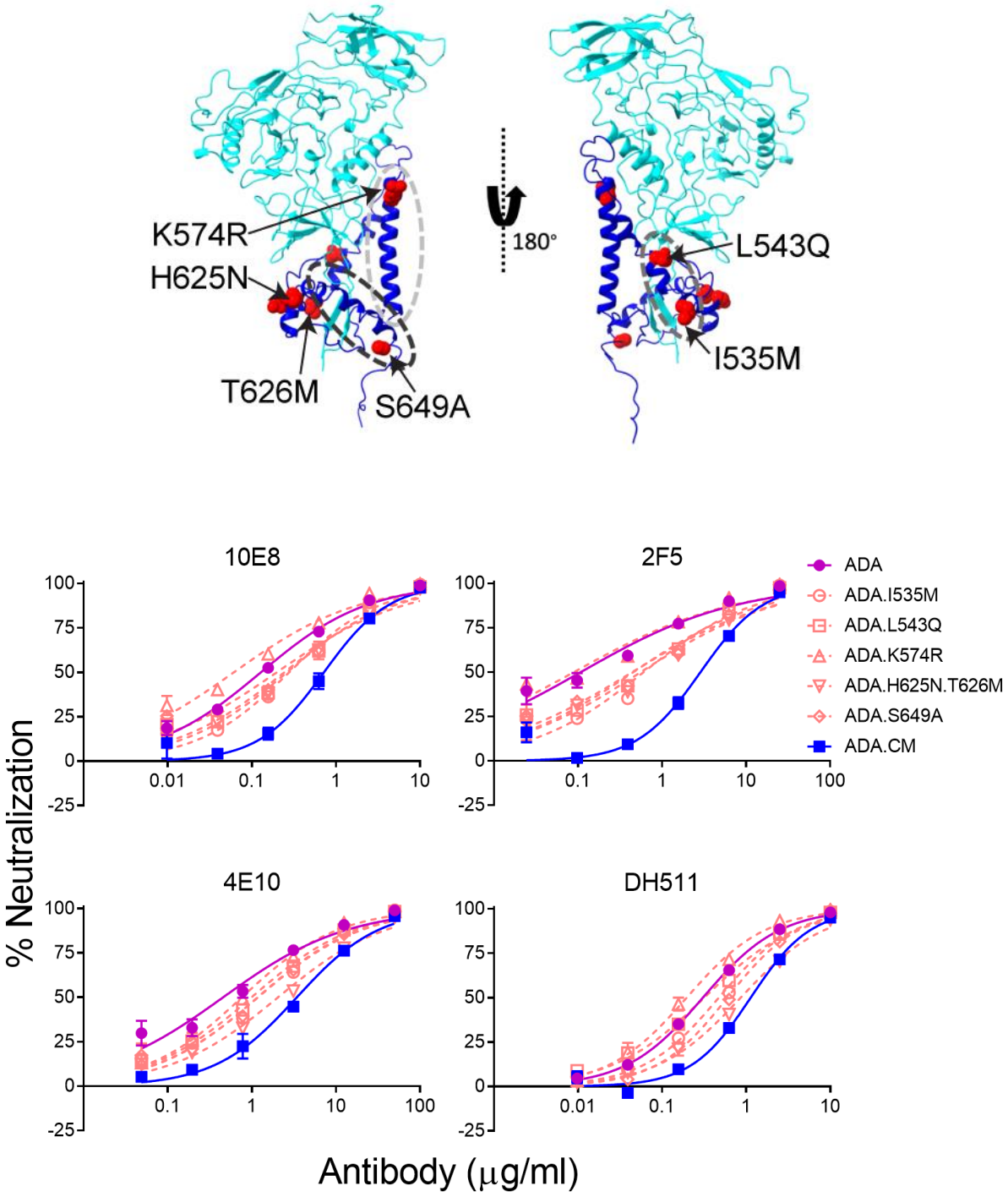

Figure S8. **Neutralization effect of individual mutations in gp41 subunit of ADA.CM with respect to MPER-targeting antibodies. Related to Figure 4.**

Top: Mutations relative to parental ADA virus in gp41 subunit that contribute to ADA.CM trimer hyperstability mapped onto its structure. The mutated residues are represented as red balls. HR1-C helix, HR2 helix and fusion loop proximal region are indicated by light grey, black and dark grey ovals respectively. Bottom: MPER antibody neutralization of single residue mutants of HIV-1 ADA in gp41 subunit, as described in Figure S14. Each ADA point mutant corresponds to residues in ADA.CM that were mutated during directed evolution of ADA to withstand destabilizing conditions (Leaman and Zwick 2013). Curves shown are from a single experiment performed in duplicate.

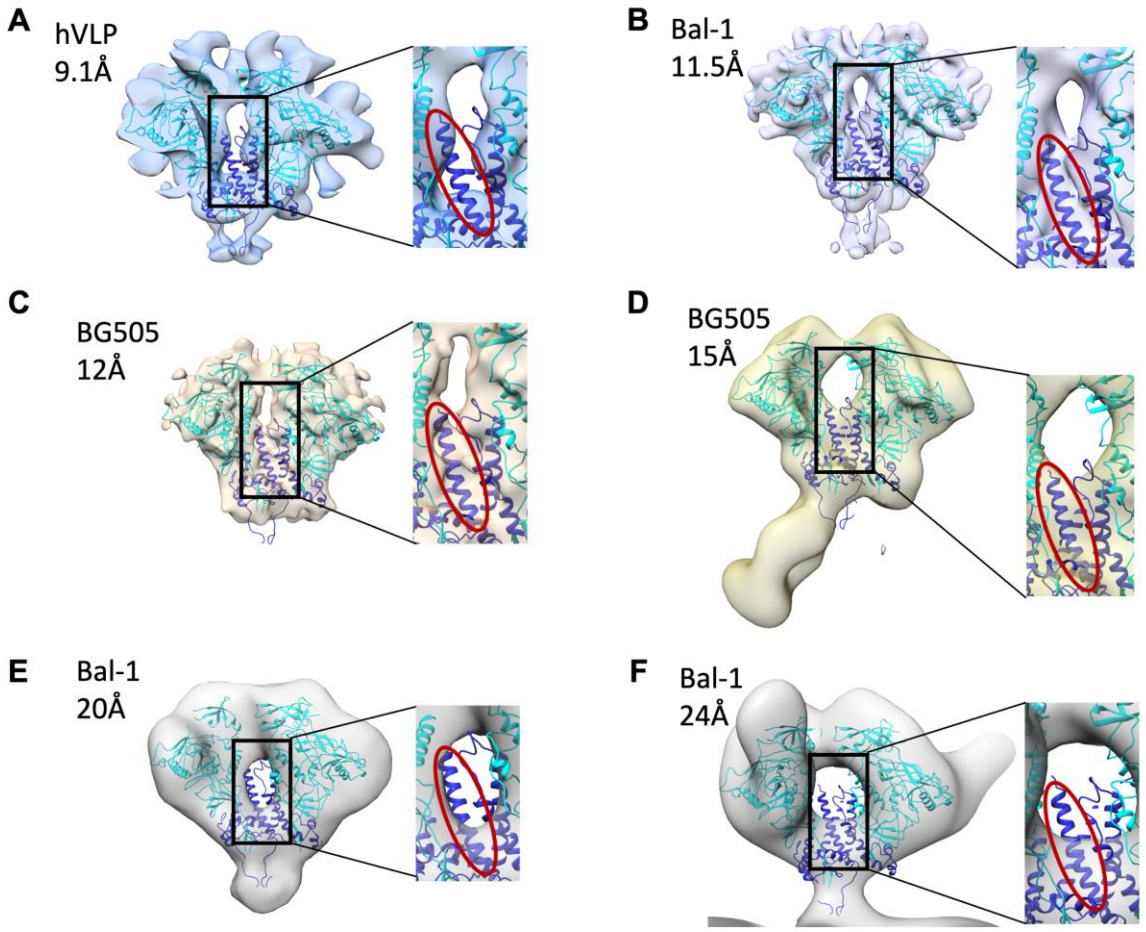

Figure S9. Comparison of HR1-C density in Env trimer structures at different resolutions. Related to Figure 5.

(**A-F**). Surface slab view of Env single particle cryo-EM and sub-tomogram averaged reconstructions with only 2 protomers shown to visualize HR1-C helix density clearly. In each panel, the central core region (black rectangle) is zoomed in and the HR1-C helix indicated with red oval. Maps shown are (A) hVLP-Env, (B) BaL-1 (EMD-21412) (Li, Li et al. 2020), (C) BG505 SOSIP.664 (EMD-5782) (Lyumkis, Julien et al. 2013), (D) BG505 SOSIP v5.2 (EMD-21075) (Cottrell, van Schooten et al. 2020), (E) BaL-1 (EMD-5019) (Liu, Bartesaghi et al. 2008), (F) Bal-1 (EMD-5457) (Tran, Borgnia et al. 2012).

Supplemental Tables:

Table S1.

Half-maximal inhibitory concentration (IC_{50}) values for antibody neutralization of VLPs displaying Envs of full-length ADA.CM, ADA.CM with truncation matching that of hVLPs (ADA.CM.755*) and high Env displaying hVLPs (ADA.CM.V4).

		ADA.CM	ADA.CM.755*	ADA.CM.V4 (hVLP)
IC_{50} (µg/ml)	VRC01	0.11	0.11	0.19
	T-20	0.020	0.020	0.024
	10E8	0.37	0.26	0.52
	DH511	0.71	0.89	1.12
	2F5	2.06	2.31	3.39
	4E10	1.87	3.57	4.64
	PGT151	0.0042	0.0032	0.0099
	35O22	0.0093	0.0019	0.0032
	8ANC195	2.51	2.10	2.98

Table S2.

IC_{50} values for neutralization of HIV-1 strains by MPER-targeted antibodies.

		ADA.CM.V4	BG505	BaL
	MPER-targeting antibodies			
IC_{50} (μg/ml)	10E8	0.46	0.16	0.21
	DH511	1.26	0.21	1.00
	2F5	2.88	0.94	1.36
	4E10	5.16	0.81	1.83
	Gp120-gp41 interface and glycan targeting antibodies			
	VRC01	0.16	0.0086	0.0028
	PGT151	0.011	0.00026	0.00083
	35O22	0.0032	>20	0.00018
	3BC176	66.7	36.5	0.93

Table S3.

IC_{50} values for neutralization of single point mutants in gp41 of ADA by MPER-targeted antibodies.

	IC_{50} (μg/ml)					
	VRC01	T20	10E8	DH511	2F5	4E10
ADA	0.31	0.016	0.13	0.31	0.11	0.46
ADA.I535M	0.36	0.013	0.28	0.47	0.60	1.17
ADA.L543Q	0.39	0.072	0.24	0.32	0.46	0.99
ADA.K574R	0.27	0.024	0.061	0.20	0.089	0.76
ADA.H625N.T626M	0.41	0.11	0.26	0.86	0.56	2.05
ADA.S649A	0.29	0.021	0.20	0.60	0.44	1.18
ADA.CM	0.16	0.013	0.72	1.13	2.86	3.43

Table S4.

N-linked glycosylation detected in hVLP-Env through peptide digest analysis by mass spectrometry.

Asn (N) residue numbers	Complex sugars[1]	Oligo-mannose[1]	Hybrid sugars[1]
88	HexNAc(4)Hex(5) HexNAc(5)Hex(5) HexNAc(5)Hex(4) HexNAc(4)Hex(5)Fuc(1)	HexNAc(2)Hex(5) HexNAc(2)Hex(4)	HexNAc(3)Hex(6) HexNAc(3)Hex(5)Fuc(1)
136	HexNAc(5)Hex(6)NeuAc(3) HexNAc(6)Hex(6)Fuc(2)NeuAc(2) HexNAc(6)Hex(7)Fuc(1)NeuAc(2)		
187/188	HexNAc(5)Hex(3)Fuc(2)		
197	HexNAc(3)Hex(4)Fuc(2)NeuAc(1)		
262		HexNAc(2)Hex(9) HexNAc(2)Hex(8)	
276	HexNAc(3)Hex(6) HexNAc(3)Hex(5) HexNAc(3)Hex(6)NeuAc(1) HexNAc(3)Hex(5)NeuAc(1)	HexNAc(2)Hex(7) HexNAc(2)Hex(6) HexNAc(2)Hex(5)	
295-301		HexNAc(2)Hex(9) HexNAc(2)Hex(5)	

332-334*	HexNAc(6)Hex(6)NeuAc(1) HexNAc(5)Hex(5)NeuAc(2) HexNAc(6)Hex(6)NeuAc(3) HexNAc(6)Hex(6)NeuAc(2)		
339	HexNAc(6)Hex(6)Fuc(2)NeuAc(2) HexNAc(5)Hex(6)Fuc(3)NeuAc(2)		
355	HexNAc(6)Hex(4)		
361	HexNAc(5)Hex(5)NeuAc(2) HexNAc(6)Hex(6)NeuAc(2)		
448	HexNAc(5)Hex(5)Fuc(2)NeuAc(1) HexNAc(6)Hex(6)Fuc(2)NeuAc(2) HexNAc(6)Hex(7)Fuc(3)NeuAc(4)	HexNAc(2)Hex(9)	
461/462	HexNAc(5)Hex(5) HexNAc(5)Hex(5)Fuc(1) HexNAc(5)Hex(4)Fuc(1) HexNAc(4)Hex(5)Fuc(1)NeuAc(1) HexNAc(5)Hex(6)Fuc(1)NeuAc(1) HexNAc(4)Hex(5)Fuc(1)		
616	HexNAc(6)Hex(6)Fuc(2)NeuAc(1)		
637			HexNAc(3)Hex(6)

* un-glycosylated peptide also observed

[1] Abbreviations and glycan classifications according to *Essentials of Glycobiology*, *3rd ed*.

HexNAc: N-acetylhexosamines; Hex: Hexose; Fuc: L-Fucose; NeuAc: N-acetyl neuraminic acid

Table S5.

Backbone carbon chain RMSD[1] in angstroms for gp120 and gp41 subunits in high resolution Env glycoprotein structures.

Gp120	92UG037.8 full length (PDB: 6ULC)	JR-FL full-length (PDB: 5FUU)	AMC011 full length (PDB: 6OLP)	BG505 SOSIP (PDB: 4ZMJ)
92UG037.8		2.204	2.980	1.752
JR-FL			1.654	1.758
AMC011				2.924
BG505				
Gp41	92UG037.8	JR-FL	AMC011	BG505
92UG037.8		5.105	4.888	3.908
JR-FL			1.928	2.063
AMC011				1.299
BG505				

[1]root mean square deviation

Table S6.

Percentage sequence similarity in Env amongst HIV-1 strains compared in Table S6.

	ADA-CM	Bal-1	JR-FL	92UG037.8	BG505
ADA-CM	100.0	84.39	88.82	76.19	76.97
Bal-1		100.0	89.78	74.68	77.29
JR-FL			100.0	76.52	76.04
92UG037.8				100.0	81.07
BG505					100.0

Supplemental References:

Cottrell, C. A., J. van Schooten, C. A. Bowman, M. Yuan, D. Oyen, M. Shin, R. Morpurgo, P. van der Woude, M. van Breemen, J. L. Torres, R. Patel, J. Gross, L. M. Sewall, J. Copps, G. Ozorowski, B. Nogal, D. Sok, E. G. Rakasz, C. Labranche, V. Vigdorovich, S. Christley, D. G. Carnathan, D. N. Sather, D. Montefiori, G. Silvestri, D. R. Burton, J. P. Moore, I. A. Wilson, R. W. Sanders, A. B. Ward and M. J. van Gils (2020). "Mapping the immunogenic landscape of near-native HIV-1 envelope trimers in non-human primates." PLoS Pathog **16**(8): e1008753.

Kucukelbir, A., F. J. Sigworth and H. D. Tagare (2014). "Quantifying the local resolution of cryo-EM density maps." Nat Methods **11**(1): 63-65.

Leaman, D. P. and M. B. Zwick (2013). "Increased functional stability and homogeneity of viral envelope spikes through directed evolution." PLoS Pathog **9**(2): e1003184.

Li, Z., W. Li, M. Lu, J. Bess, C. W. Chao, J. Gorman, D. S. Terry, B. Zhang, T. Zhou, S. C. Blanchard, P. D. Kwong, J. D. Lifson, W. Mothes and J. Liu (2020). "Subnanometer structures of HIV-1 envelope trimers on aldrithiol-2-inactivated virus particles." Nat Struct Mol Biol **27**(8): 726-734.

Liu, J., A. Bartesaghi, M. J. Borgnia, G. Sapiro and S. Subramaniam (2008). "Molecular architecture of native HIV-1 gp120 trimers." Nature **455**(7209): 109-113.

Lyumkis, D., J. P. Julien, N. de Val, A. Cupo, C. S. Potter, P. J. Klasse, D. R. Burton, R. W. Sanders, J. P. Moore, B. Carragher, I. A. Wilson and A. B. Ward (2013). "Cryo-EM structure of a fully glycosylated soluble cleaved HIV-1 envelope trimer." Science **342**(6165): 1484-1490.

Mattei, S., A. Tan, B. Glass, B. Müller, H. G. Kräusslich and J. A. G. Briggs (2018). "High-resolution structures of HIV-1 Gag cleavage mutants determine structural switch for virus maturation." Proc Natl Acad Sci U S A **115**(40): E9401-E9410.

Tran, E. E., M. J. Borgnia, O. Kuybeda, D. M. Schauder, A. Bartesaghi, G. A. Frank, G. Sapiro, J. L. Milne and S. Subramaniam (2012). "Structural mechanism of trimeric HIV-1 envelope glycoprotein activation." PLoS Pathog **8**(7): e1002797.